REPORT NO. DOT - TSC - NASA -71 - 7

# MILLIMETER-WAVE GENERATION WITH SPIRALING ELECTRON BEAMS

BERNHARD KULKE



# TRANSPORTATION SYSTEMS CENTER

## 55 BROADWAY CAMBRIDGE, MA 02142

FEBRUARY 1971

TECHNICAL REPORT

Prepared for

NATIONAL AERONAUTICS AND SPACE ADMINISTRATION
WASHINGTON, D. C. 20590

| 1. Report No. | 2. Government Accession No. | 3. Recipient's Catalog No. |
|---|---|---|

| 4. Title and Subtitle | 5. Report Date |
|---|---|
| Millimeter-Wave Generation with Spiraling Electron Beams | February 1971 |
| | 6. Performing Organization Code |
| | TER |

| 7. Author(s) | 8. Performing Organization Report No. |
|---|---|
| Bernhard Kulke | DOT-TSC-NASA-71-7 |

| 9. Performing Organization Name and Address | 10. Work Unit No. |
|---|---|
| Transportation Systems Center | NA-10 |
| 55 Broadway | 11. Contract or Grant No. |
| Cambridge, MA 02142 | |
| | 13. Type of Report and Period Covered |
| 12. Sponsoring Agency Name and Address | |
| National Aeronautics and Space Administration | Technical Report |
| Washington, DC 20590 | 14. Sponsoring Agency Code |
| | R1058 |

15. Supplementary Notes

16. Abstract

An investigation has been carried out of the feasibility of using the interaction between a thin, solid, spiraling electron beam of 10-20kV energy and a microwave cavity to generate watts of CW millimeter-wave power. Experimental results are given for several prototype devices operating at 9.4 GHz and at 94 GHz. Power outputs of 5W, and electronic efficiencies near 3%, were obtained at X-band, and moderate gain was obtained at 94 GHz. The small-signal theory gives a good fit to the X-band data, and the device behavior at 94 GHz is as expected from the given beam characteristics. The performance is limited chiefly by the velocity spread in the spiraling electron beam, and once this can be brought under control, high-power generation of millimeter waves appears quite feasible with this type of device.

| 17. Key Words | 18. Distribution Statement |
|---|---|
| .Spiraling Electron Beam<br>.Microwave Cavity<br>.9.4 and 94 GHz<br>.High-Power Millimeter Waves | Unclassified — Unlimited |

| 19. Security Classif. (of this report) | 20. Security Classif. (of this page) | 21. No. of Pages | 22. Price |
|---|---|---|---|
| Unclassified | Unclassified | 98 | |

# ACKNOWLEDGEMENTS

CONTENTS

# 1. INTRODUCTION

This report summarizes the results of an exploratory research and development program involving spiraling-beam oscillators for use at mm and sub-mm wavelengths. This program was initiated at the NASA/Electronic Research Center in July 1967, and completed in December 1970, within the framework of the Transportation Systems Center, Department of Transportation, though still under NASA sponsorship.

Spiraling-beam oscillators (or amplifiers) are devices in which an ensemble of energetic electrons orbiting in a uniform magnetic field is exposed to an r.f. electric field vector at right angles to the electron axis of rotation. The r.f. field vector itself rotates at a rate slightly faster than the electrons, and the Lorentz force on the randomly phased electrons, together with a slight relativistic mass dependence on the velocity, produces a net bunching of the electrons into the decelerating phase of the r.f. field vector, which is necessary to obtain electronic gain. In the case of an oscillator, the gain is great enough to overcome the ohmic losses of the system, and thus the electric field becomes self-excited and will increase until limited by non-linear effects in the beam-field interaction.

The decision to investigate spiraling-beam oscillators as potential high-power mm-wave sources was based on a comprehensive survey conducted in 1966 of electron-beam techniques used for mm-wave generation (Ref. 1).

This survey indicated that while ultra-miniature mm-wave versions of conventional traveling-wave tubes and backward-wave oscillators were either available or being developed commercially, the power output of these tubes decreased very rapidly with frequency, so that as of 1966, there were virtually no tunable sources available which would produce more than 0.1 W between 300 and 1000 GHz. Figure 1.1 gives a more recent set of data, which has remained essentially unchanged today. Those tubes that do function in this frequency range are difficult to manufacture, very costly, and relatively short-lived.

Research then in progress indicated that alternative means of high-frequency power generation could eventually become available in off-the-shelf form, for example, avalanche diodes or cyanide lasers. Meanwhile, spiraling-beam (or fast-wave) devices, though seemingly quite promising, had never really left the realm of university laboratories. Some encouraging experimental results at S and X band frequencies (Ref. 2, 3) and at 135 GHz (Ref. 4) were augmented by analytical work stressing the physical model of the interaction mechanism (Refs. 5-9) but with one exception, industry showed little interest in further development of the devices. Work on Bott's tube (Ref. 4) was pursued (Ref. 10) at the Mullard Research Laboratories, England, for about a year after Bott had published his results. Impressive results were reported in the Russian literature, for example, (Ref. 11). However, as the Russian
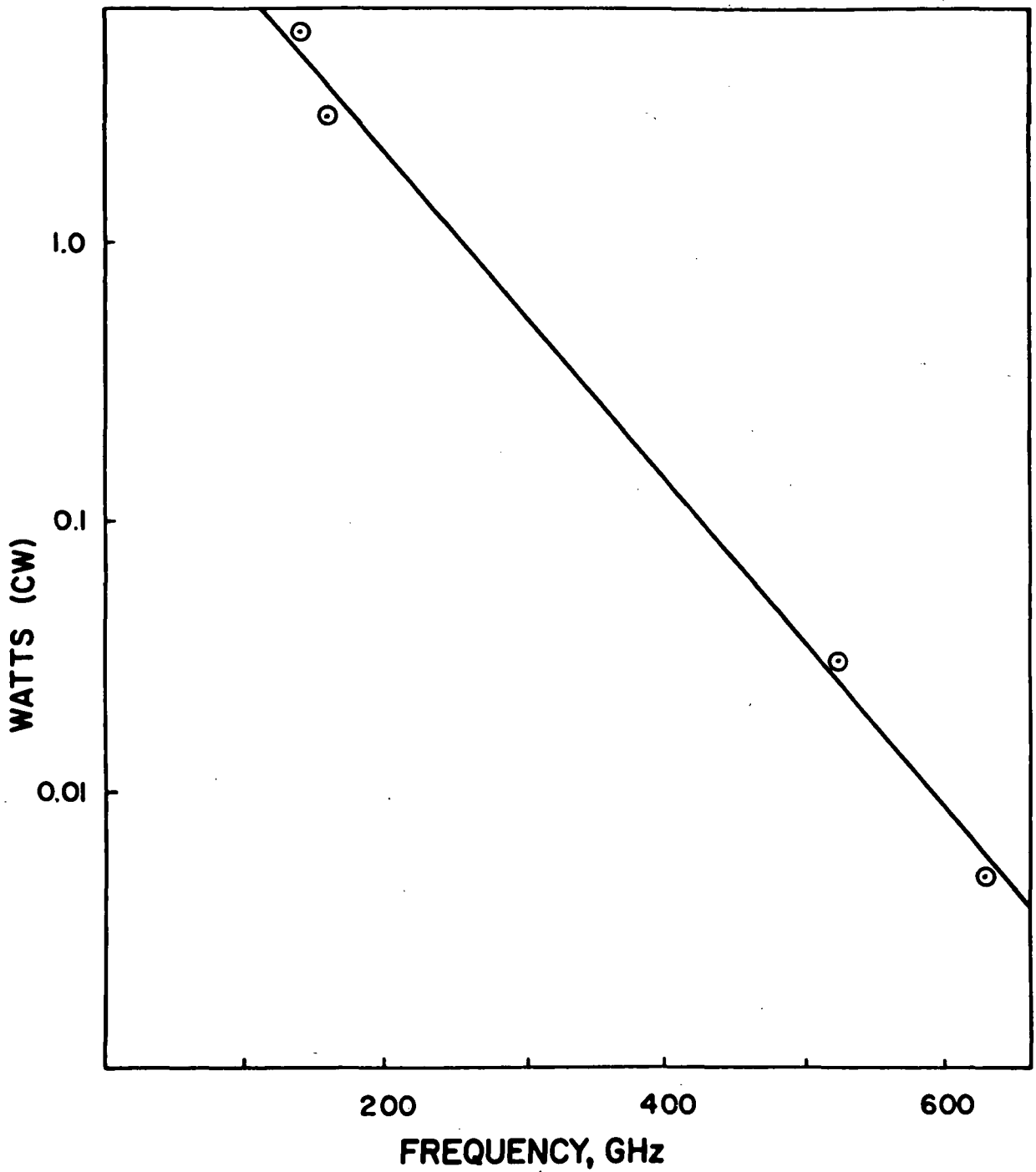
Figure 1.1- Max. cw power output vs frequency, quoted for a leading commercial line of backward-wave oscillators, using solenoid focusing.  (Data taken from <u>Micro-waves</u>, vol. 9, Sept. 1970, p. 27.)

authors appear to be rather reticent about giving either complete derivations of their mathematical expressions or details of their experimental method, their papers proved to be of little help in understanding the underlying physical mechanism. A summary of the important experimental results reported in the literature is given in Table 1.1. From the viewpoint of accomplishing a significant experiment requiring a minimum of support facilities and equipment, Bott's simple technique (Ref. 4) looked particularly attractive, and thus it became essentially the starting point of the work reported here.

The objective was to produce easily usable design information and to probe for the upper bounds on power and frequency. The long-range experimental plan was to include eventually both spiraling cylindrical and trochoidal sheet beams, in both traveling-wave and standing-wave field configurations. Time and manpower constraints later limited the work to an investigation of devices utilizing thin, solid, spiraling electron beams in conjunction with cavity resonators; however, many of the insights gained should apply equally to other types of periodic beams interacting with fields supported by smooth (non-periodic) metallic structures. In particular, it turned out that the energy spread on the periodic electron beam emerges as probably the most important limitation on the efficiency. This important fact has been thoroughly investigated both theoretically and experimentally during the course of this work.

TABLE 1.1.- COMPARISON OF EXPERIMENTAL PARAMETERS FOR SOME CYCLOTRON RESONANCE OSCILLATORS

| Experiment | Bott (Ref. 4) | Hirshfield Bernstein and Wachtel (Ref. 9) | Gaponov, et al. (Ref. 11) | Schriever and Johnson (Ref. 3) | Antakov, et al. (Ref. 12) |
|---|---|---|---|---|---|
| Type of gun | Pierce gun immersed | Parallel-plane diode, immersed | Conical cathode | Magnetron injection gun | Kino gun |
| Electron Trajectory | Spiral | Spiral | Spiral | Spiral | Cycloid |
| Beam voltage | 20 kV | 5 kV | 19 kV | 10 kV | 14 kV |
| Cathode current | 25 mA | 50 mA | 320 mA | 1300 mA | 600 mA |
| Type of trajectory modulation | Corkscrew | Corkscrew | Crossed-field injection | Crossed-field injection | Crossed-field injection |
| Type of interaction | Combination resonant and backward-wave Circular $TE_{mn}$ | Resonant, circular $TE_{011}$ | Resonant, circular $TE_{021}$ | Backward-wave | Backward-wave |
| Power | 1 W | 10 mW | 190 W | 720 W | 850 W |
| Frequency | 143 GHz | 5.8 GHz | 25 GHz (2nd harmonic) | 9 GHz | 38 GHz |
| Efficiency* | 0.2% | - | 3% | 6% | 10% |

*Some ambiguity exists dependong on weather cathode or collected current should be used as a base. In this Table, cathode current is used.

The present report is organized into five sections. Following the introduction, an analytical treatment of the inter- action of a spiraling electron beam with a microwave field is presented. This is followed by a discussion of the methods of beam formation that were used in this work. Experimental results obtained from actual devices are followed by the overall con- clusions. Where appropriate, capsule summaries are appended to the individual sections.

2. THE INTERACTION OF A SPIRALING ELECTRON BEAM WITH A MICRO-
   WAVE FIELD

In this discussion two different mathematical models for
beam-field interaction are considered, one corresponding to a
traveling-wave and the other to a standing-wave environment.
The latter model will be explored in greater detail, and calcu-
lations will be presented that illustrate the more important
design tradeoffs. Detailed comparison with experimental data
is deferred to a later portion of this report, so as not to
burden the more general picture given here.

2.1  Interaction with a Traveling Wave

Spiraling-beam interaction with an electromagnetic wave
supported by a smooth, hollow, metallic waveguide has been
analyzed by a number of authors; at first without allowing for
any relativistic mass change of the moving electrons (Refs. 5,
6), and later including a relativistic correction (Refs. 7,
13-16). It was found that the latter forms a rather crucial
part in a complete description of the interaction mechanism,
despite the fact that the electron energies are not in the range
where one would ordinarily consider relativistic effects.

A sketch of the physical configuration is given in Figure
2.1. A section of smooth, hollow waveguide supports an electro-
magnetic wave propagating from left to right, e.g., in the
dominant rectangular TE (10) mode. A beam of randomly phased,
spiraling electrons enters the waveguide axially. In order for
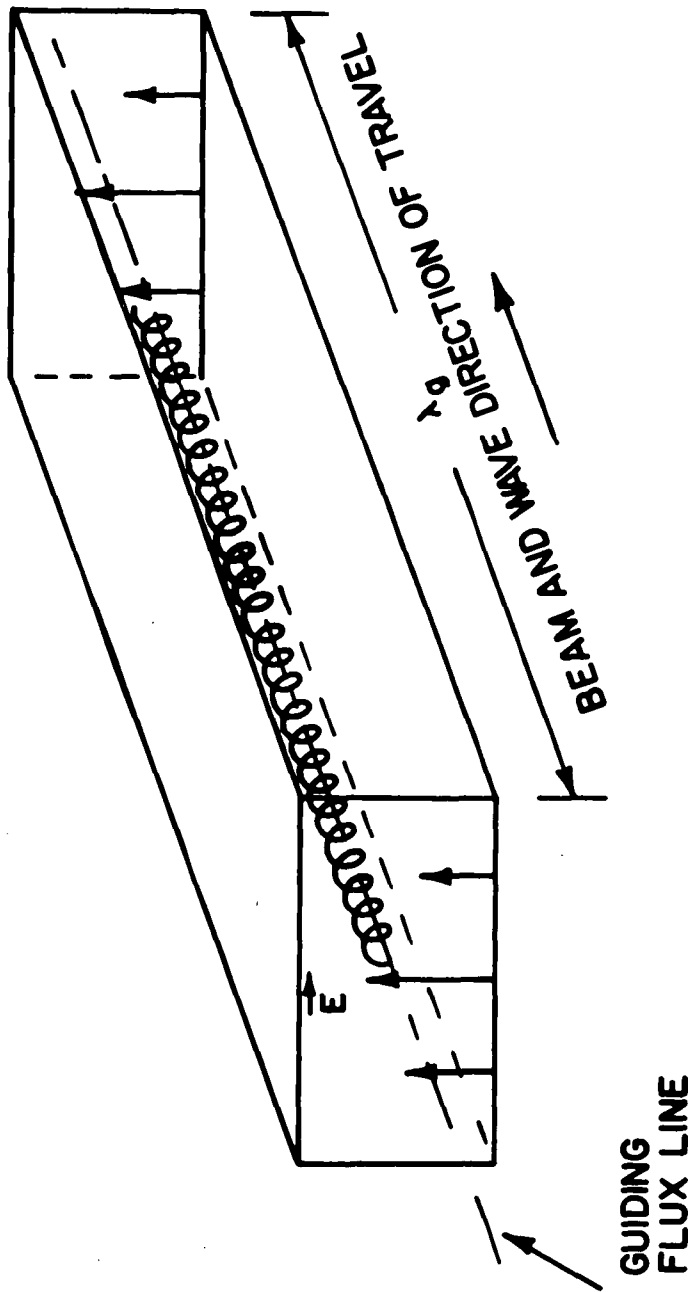interaction to take place, some sort of synchronism must first

Figure 2.1.- Physical configuration of spiraling-beam interaction with a traveling
wave in the TE(10) rectangular mode.

be established between the electric field vector, varying as
$\exp(-j)(\omega t - k_{11}z)$ and the transverse velocity vector varying as
$\exp(-j)(\Omega t)$ where:

$\Omega = \dfrac{eB}{m}$ = the cyclotron frequency

$\omega$ = field frequency

$k_{11} = \dfrac{\omega}{v_p}$ wave propagation constant

$u_o$ = axial velocity of the electrons

$v_p$ = phase velocity of the field pattern

Direct synchronism would require $u_o = v_p > c$, which is
physically impossible. Instead, the field wave is allowed to
"move through" the much slower pattern of electrons. That is,
by setting $\Omega T = \omega T - k_{11}L$, where L is the small axial distance
traveled by an electron during one r.f. period T, one obtains the
so-called d.c. synchronism condition, given by:

$$\Omega = \omega \left( \frac{1-u_o}{v_p} \right) \tag{2.1}$$

In actual operation, the cyclotron frequency $\Omega$ is set
slightly below this value. The resultant frequency difference
$\left( \dfrac{\Omega - \omega}{\omega} \right)$ will be called the slip rate.

If net power is to be transferred from the beam to the field, the randomly phased electrons must be sorted, or bunched, such that a majority of them begin and continue to move in the retarding phase of the electric field. There are in fact two different bunching mechanisms. The first is due to an axial Lorentz force that arises from the transverse velocity component in conjunction with the transverse r.f. magnetic field component. Although the force is axial, the resultant bunching along the helical electron trajectory is still, in effect, circumferential. This mechanism is strongest far away from the waveguide cutoff frequency, and it vanishes near cutoff as the transverse magnetic field component goes to zero.

The second bunching mechanism arises from the relativistic mass change (and the resultant change in the cyclotron frequency) of electrons as they are accelerated or retarded by the transverse electric field component. The change in the orbit frequency serves to increase or decrease the initially existing slip rate between the field and the moving electron, and the beam can be made to either absorb energy from or to give up energy to the electric field, depending on the direction of the initial slip. Unlike the Lorentz-force bunching, the relativistic bunching mechanism does not vanish near waveguide cutoff. In analyses where both mechanisms have been included (Refs. 13, 14, 15), there arises a factor $\left(1 - \dfrac{\omega_c^2}{\omega^2}\right)$ which is proportional to the ratio of the Lorentz bunching to the relativistic bunching rates,

i.e., the respective time derivatives of angular frequency. Clearly, the Lorentz bunching vanishes as the operating frequency $\omega$ approaches the cutoff frequency $\omega_c$, whereas the relativistic mechanism becomes stronger.

All the available closed-form analyses of spiraling beam-traveling wave interaction, restrict themselves to the small-signal regime, either implicitly by using a coupled-mode approach (Refs. 5, 6, 13-15) or by linearizing the formidable equations generated from a ballistic approach (Refs. 7, 16). Large-signal numerical integration of the equations of motion has been carried out in two cases, one to predict Bott's results (Ref. 7) and another to compare with Kulke's early experimental data (Refs. 17, 18).

In order to keep the large-signal expressions tractable for computation, series expressions were truncated beyond the second-order terms, and neither analysis allows for the presence of velocity spread on the beam. However, both papers provide an informative study of the electronic gain mechanism.

2.2   Interaction with a Standing Wave

When the waveguide section of Figure 2.1 is closed off with a metallic shorting plane on either or both ends, a standing wave results. (Small holes allow the beam to pass through the end planes.) The physical situation now resembles the electric field of an r.f. - driven capacitor acting on the beam, i.e.,

the device becomes a Cuccia coupler with axially varying field intensity. The Lorentz force due to the r.f. magnetic-field component changes polarity every half cycle and so has negligible effect. The resulting interaction was first analyzed by Schneider (Ref. 19) in quantum-mechanical terms, and in greater detail, classically, by Hsu and Robson (Ref. 8), and by Hirshfield, Bernstein, and Wachtel (Ref. 9). This last paper forms the starting point of much of the analytical work in this report, and hence it will be outlined below in greater detail.

The approach of Hirshfield, et al., starts from statistical mechanics, and this permits one to take into account a finite-width velocity distribution among the electrons. This analytical technique offers a great advantage over other analyses mentioned before, because of the importance of the velocity spread on the beam. The electron beam inside the interaction region is considered as an axially drifting, ion-neutralized column of electrons, with each electron orbiting at the cyclotron frequency about a magnetic flux line. Given the d.c. electron velocity distribution, the linearized Boltzmann-Vlasov equation is then solved for the perturbed (a.c.) part of the distribution function in terms of the known electromagnetic field components within the interaction region. Only the transverse electric field component is retained as significant. For the case of the TE(011) cylindrical resonator discussed by Hirshfield, et al., this is given by the following:

$$\vec{E}_1 = \vec{a}_\theta \, E_o J_1(k_\perp r) \, \sin k_{11} z \, \cos \omega t \qquad\qquad (2.2)$$

The r.f. convection current density $\vec{J}$ follows by integrating over the electron velocity distribution, and the power flow from the beam to the r.f. electric field $\vec{E}_1$ is derived by integrating the $\vec{J} \cdot \vec{E}$ product over the interaction space. (It is assumed that the rf field configuration is identical to that which would exist in the absence of the beam.) The result is, for a sinusoidal axial field variation:

$$P = \frac{\pi}{4} \, \frac{e^2 E_o^2}{m k_{11}^2} \, \rho(k_\perp a) \int dw \int du \; h_0(u,w)$$

$$\cdot \; \frac{w^3}{u^3} \cdot \frac{2 k_{11} u}{\omega} \; G(x) \left[ \frac{\omega}{k_{11} c} \cdot \frac{uc}{w^2} + Q(x) \right]$$

$$(2.3)$$

where

$$x = \frac{\Omega - \omega}{k_{11} u}$$

$$G(x) = \frac{\cos^2\left(\frac{\pi x}{2}\right)}{\left(1 - x^2\right)^2}$$

$$Q(x) = x - \frac{1}{2G(x)} \frac{dG}{dx} \left( \frac{\omega^2}{k_{11}^2 c^2} - x^2 \right)$$

where

$\Omega$ = cyclotron frequency

$\omega$ = frequency of r.f. field

$k_{11} = \dfrac{2\pi}{\lambda_g}$ = axial propagation vector

$k_{\perp}$ = transverse propagation vector

$w,u$ = transverse, axial velocity

$E_o$ = magnitude of r.f. electric field vector

$h_o(u,w)$ = unperturbed velocity distribution function

The quantity $\rho(k_{\perp}a)$ represents the electron number density N weighted by the transverse electric field variation over the beam cross-section. For example, if the interaction takes place in the strong electric field region of a $TE_{011}$ cylindrical cavity, then:

$$\rho(k_{\perp}a) = \int_{\text{beam area}} J_1^2(k_{\perp}r)\ N(r,\theta)\ dA$$

Clearly, the interaction mechanism is described by the double integral term in Eq. (2.3). If a mono-energetic beam is assumed, the velocity distribution becomes a double delta function:

$$h_o(u,w) = \frac{1}{2\pi w_o}\ \delta(u-u_o)\ \delta(w-w_o) \tag{2.4}$$

where the term in the denominator arises from the necessary velocity-space normalization of the distribution function in cylindrical coordinates. Equation (2.3) then becomes:

$$P = \frac{eE_o^2}{4_m k_{11}^2 u_o} \, \rho(k_\perp a) \, G(x) \, (1 + \beta Q(x)) \qquad (2.5)$$

where

$$\beta \equiv \frac{k_{11}c}{\omega} \cdot \frac{w_o^2}{u_o c}$$

The so-called gain function $G(x)(1+\beta Q(x))$ here describes the basic interaction. It should be noted that for a given set of velocities $(u_o, w_o)$, the ratio $k_{11}/k \equiv \sqrt{1 - \lambda^2/\lambda_c^2}$ enters as a parameter both through $\beta$ and through the function $Q(x)$. In Figures 2.2 and 2.3 we have plotted the gain function vs x with both $\beta$ and $k_{11}/k$ as a parameter, in order to emphasize its dependence on *both* the transverse energy and on the proximity to waveguide cutoff.

The paper by Hirshfield, et al., shows only a plot similar to Figure 2.2, and an unwary reader may miss the importance of the $k_{11}/k$ dependence. The region of greatest interest is x < 0 where the gain function goes negative, indicating that power is emitted by the beam. Clearly, the electronic gain increases both with increasing transverse energy and with closer proximity to cutoff. Physically, the latter dependence simply reflects the fact that in a cavity resonator, the transverse electric field component, with a sinusoidal axial variation, always extends over a distance of one-half guide wavelength. The theoretical cavity
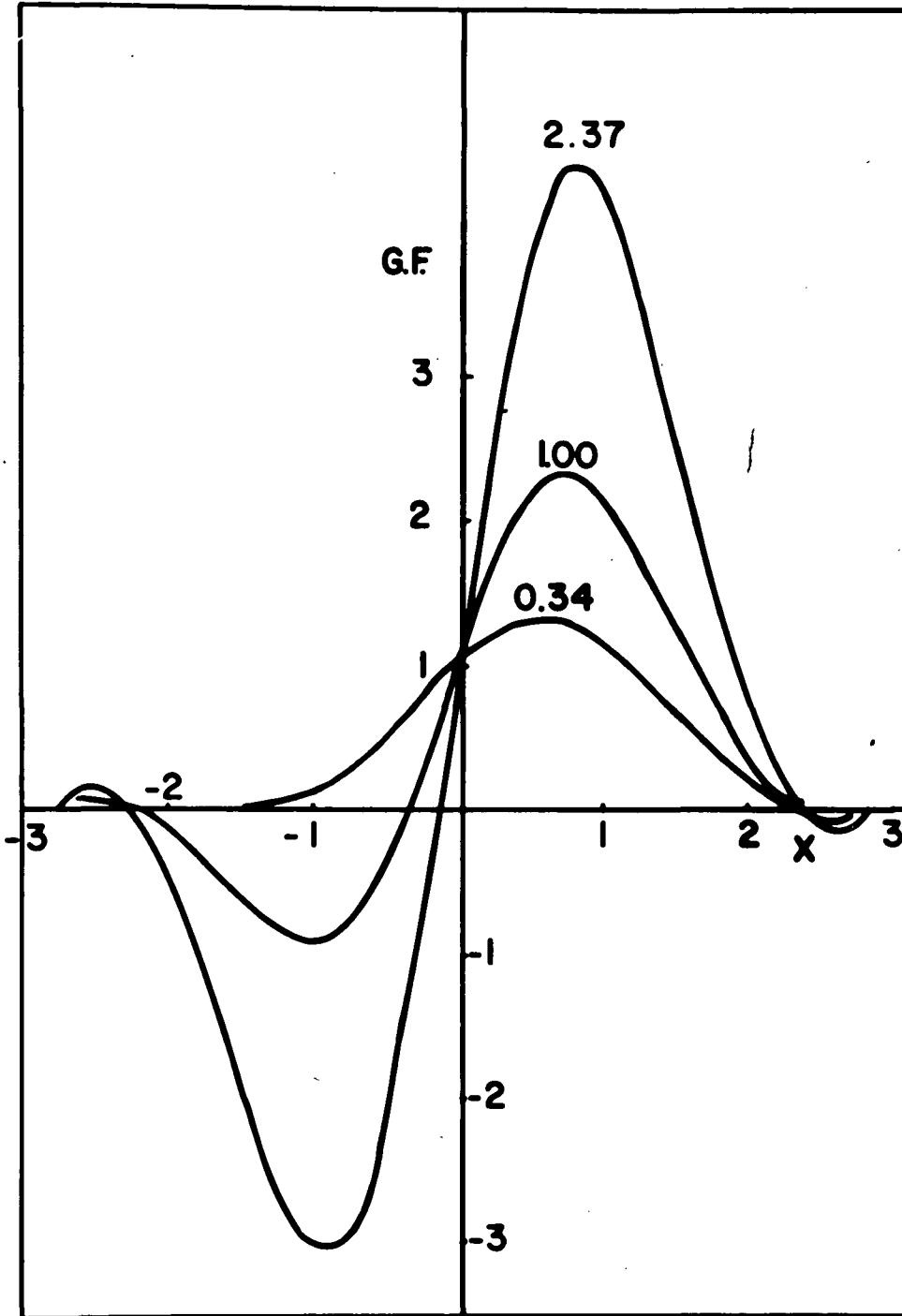
Figure 2.2.- The Gain Function $G(x)[1+\beta Q(x)]$ plotted vs $x = \frac{\Omega-\omega}{k_{11}u_o}$, with $k_{11}/k=0.5$. The parameter is $\beta \equiv \frac{k_{11}c}{\omega} \cdot \frac{w_o^2}{u_o c}$.

length increases without bound as $k_{11}/k$ decreases, and so the electrons get to spend more and more time in the interaction region, for a given axial drift velocity.

In both Figures 2.2 and 2.3, the gain function is seen to reach a negative maximum near x = -1, corresponding to the maximum amount of r.f. power being extracted from the beam. This condition can be written as:

$$x \equiv \frac{\Omega - \omega}{k_{11} u_o} = \frac{\Omega - \omega}{\omega} \cdot \frac{c}{u_o} \cdot \frac{1}{\sqrt{1-\lambda^2/\lambda_c^2}} \cong (-1) \qquad (2.6)$$

The standing-wave pattern in the cavity resonator can be expressed as two oppositely-traveling wave components. The phase velocity of either component is given by:

$$v_p = \frac{c}{\sqrt{1-\lambda^2/\lambda_c^2}}$$

and this leads to the condition for the maximum-gain, given by the expression:

$$\Omega \cong \omega \left(1 - \frac{u_o}{v_p}\right) \qquad (2.7)$$

Equation 2.7 is identical to the d.c. synchronism condition for traveling-wave interaction, Eq. (2.1), consequently, leading to the conclusion that the standing-wave interaction is really an interaction with one traveling-wave component of relatively
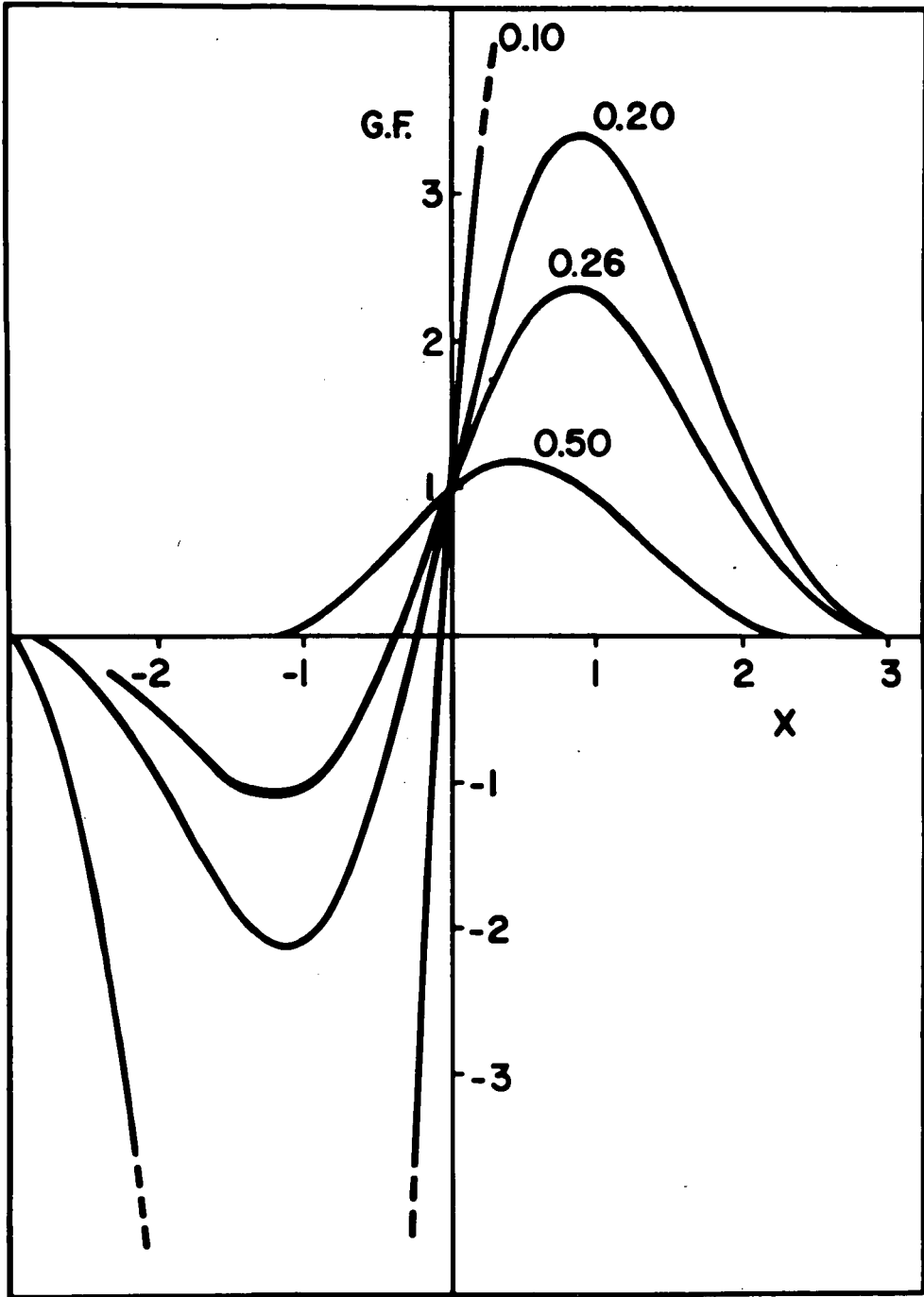
Figure 2.3.- The Gain Function $G(x)[1+\beta Q(x)]$ plotted vs $\frac{\Omega-\omega}{k_{11}u_o}$, with $\beta=0.34$. The parameter is $k_{11}/k$.

high amplitude over a relatively short distance.  An analogy is possible with a linear-beam klystron cavity of the extended-interaction type (Ref. 20).  Another conclusion that can be derived is the following.  It should be possible to increase the length of the interaction region of a well-behaved beam by an arbitrary number of resonant half-wavelengths, and thereby to increase the efficiency of the interaction.  Bott's successful experiments (Ref. 4) did in fact use a multi-wavelength, low-Q resonator, although his resonant modes were never clearly identified.

The dependence on the transverse beam energy (essentially, eVo) of the mono-energetic gain function is linear.  This follows directly from Eq. (2.5), as $\beta$, and hence the gain, increases linearly with transverse energy.

It will be evident from Figures 2.2 and 2.3, that a threshold value exists for both $k_{11}/k$ and $\beta$ below which it is impossible to get electronic gain.  For example, with $k_{11}/k = 0.5$, one must have $\beta > 0.34$, and with $\beta = 0.34$, one must have $k_{11}/k < 0.5$ in order to get gain.  In practice, the cavity would be designed as close to waveguide cutoff as possible, thereby fixing the value of $k_{11}/k$.  This, in turn, defines a threshold on $\beta$ and, hence, on $w_o^2/c^2$, the minimum value of transverse energy that will produce gain.  In order to deduce $w_o^2/c^2$ from the known $\beta$, a reasonable value of $u_o/c$ must be assumed.  In Figure 2.4, we have plotted the threshold value of transverse energy
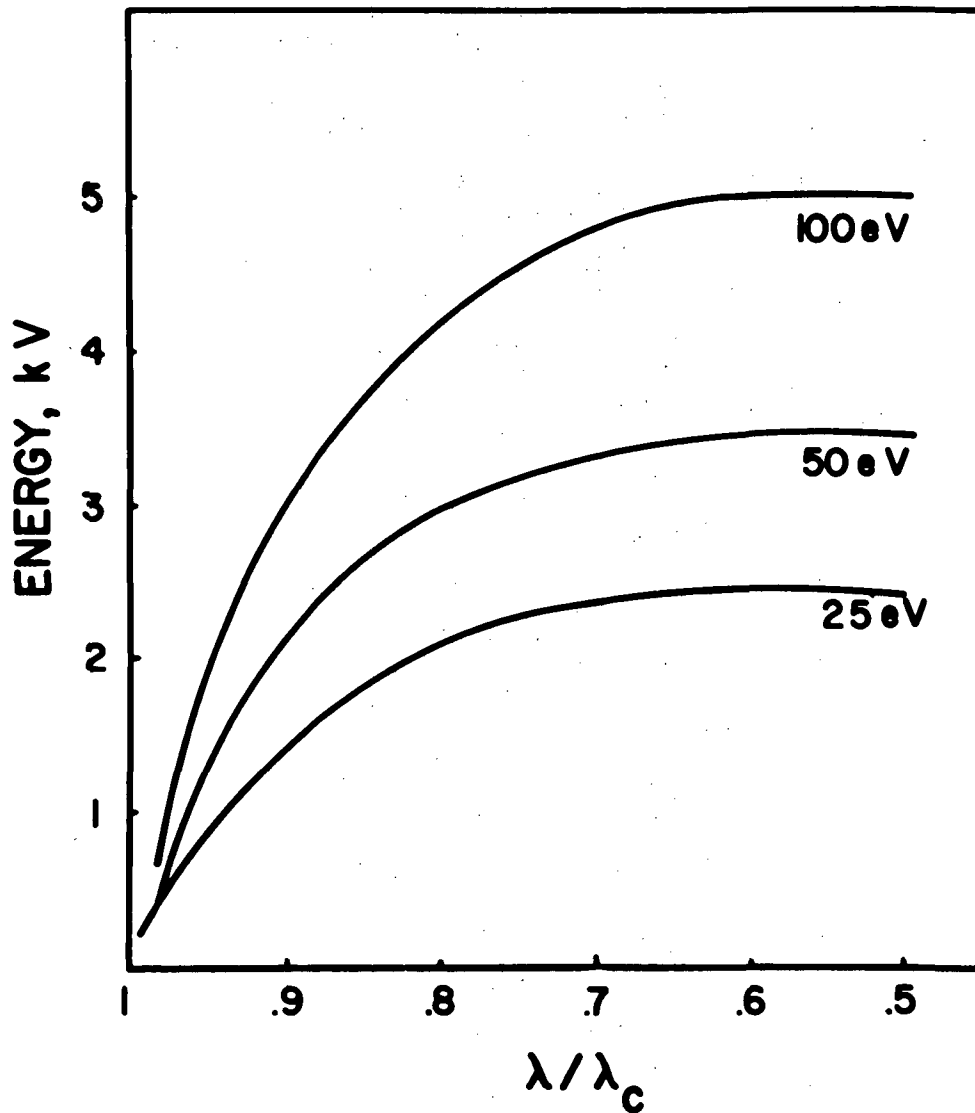
Figure 2.4.- Threshold value of transverse energy plotted vs $\lambda/\lambda_c$, where $\lambda_c$ is the cutoff wavelength of the waveguide resonator. The parameter is the energy of axial motion of the electrons.

vs $\lambda/\lambda_c$, with the energy of axial motion as a parameter. The values chosen for the latter represent a realistic operating range. From Figure 2.4, it is seen that the energy threshold will be minimized by operating close to waveguide cutoff and by using a beam with a low axial drift velocity. In practice, the beam is not mono-energetic, of course, and the electron energies are spread out over a finite range. The electronic gain will be less than that of the mono-energetic beam and the gain threshold for the (average) transverse energy will be higher. The following section will be devoted to a more detailed study of the gain behavior when there is finite velocity spread present on the beam.

## 2.3 Interaction with a Standing Wave in the Presence of Velocity Spread

In this section, the expressions analogous to the gain function $G(x)$ $(1 + \beta Q(x))$, will be derived in a form that is valid for a beam of spiraling electrons that are distributed over a finite range of axial and transverse energy. Going back to Eq. (2.3), it will be recalled that the gain mechanism is described by a double integral over velocity space. For a mono-energetic beam, this integral becomes, trivially:

$$\iint du\ dw\ (\cdots) = \frac{G(x)}{\pi u_o}\ (1 + \beta Q(x)) \qquad (2.8)$$

In following the notation of Hirshfield et al., the factor $1/\pi u_o$ was suppressed in discussing the mono-energetic gain function

$G(1 + \beta Q)$ of the previous Section. For a beam with finite velocity spread, however, the double integration is no longer trivial and all terms must be included. In order to obtain convenient numbers, we shall define and calculate a normalized gain function:

$$N.G.F. \equiv c \iint (\cdots) \, du \, dw \qquad\qquad (2.9)$$

where c is the velocity of light *in vacuo*.

The actual form of the distribution is, of course, closely tied to the method of generating the beam. The beams used in the experimental devices are described in another section. Direct measurements on a typical beam showed that the axial velocity distribution was sufficiently flat-topped so that a simple rectangular form constitutes a reasonable approximation, given by:

$$f(u) = f_o, \quad u_o \leq u \leq u_1 \qquad\qquad (2.10)$$

over a range $\Delta u = u_1 - u_o$. If one assumes that the overall distribution can be represented as a simple product:

$$h(u,w) = f(u)g(w) \qquad\qquad (2.11)$$

then normalization requires that, in cylindrical velocity space:

$$\iint 2\pi w \, du \, dw \, f(u)g(w) = 1 \qquad\qquad (2.12)$$

2-16

Substituting Eq. (2.10) we find:

$$g(w) = \frac{g_o}{2\pi w}, \quad w_o \leq w \leq w_1 \tag{2.13}$$

where $g_o$ is a constant, and finally:

$$f_o g_o = \frac{1}{(u_1 - u_o)(w_1 - w_o)} \equiv \frac{1}{\Delta u \Delta w} \tag{2.14}$$

The definition of $g(w)$, Eq. (2.13) reflects the fact that as electrons are crowded out of an axial velocity range $\Delta u$ by adiabatic conversion of momentum, they fall into an annular area $2\pi w dw$ in a transverse plane of velocity space, and thus the density $g(w)$ decreases as $w$ increases.

Substituting Eqs. (2.10) and (2.13) into Eq. (2.9) and dropping the minus sign in front, the following is obtained for the normalized gain function:

$$N.G.F. = \frac{c}{\pi \Delta u} \left\{ \int_{x_o}^{x_1} \frac{G(x)}{x} dx + K_2 \int_{x_o}^{x_1} G(x)Q(x)dx \right\} \tag{2.15}$$

where

$$K_2 \equiv \left(\frac{\omega}{\Omega - \omega}\right)\left(1 - \frac{\lambda^2}{\lambda_c^2}\right)\left(\frac{w_1^2}{3_c^2}\right)\left(1 + \frac{w_o}{w_1} + \frac{w_o^2}{w_1^2}\right).$$

and the limits $x_o$, $x_1$ correspond to $u_o$, $u_1$ respectively. As a check on Eq. (2.15), we note that it reduces to Eq. (2.8) for

the mono-energetic case. The integrals involving G(x) and Q(x) were calculated numerically, and the normalized gain function has been plotted as a function of the negative slip rate, $\frac{\omega - \Omega}{\omega}$, in Figures 2.5 and 2.6. The parameters $\lambda/\lambda_c$ and $V_o$ were chosen as actual values corresponding to an X-band experimental device. A rectangular velocity distribution has been assumed, extending from the origin to some finite value. However, in order to get agreement with the gain behavior observed experimentally, the assumption is made that the slowest electrons (axially) are excluded from the r.f. interaction, presumably because of d.c. space-charge effects to which these electrons are most susceptible. A lower limit of 15eV was found to give a reasonably good fit to the experimental results, and the curves in Figure 2.5 have been calculated with this assumption. The gain curves plotted in Figure 2.6 illustrate the effect of moving the lower limit of the energy range contributing to gain. Clearly, the gain increases when the distribution is moved closer to the origin. This behavior is similar to that of the gain function calculated for a mono-energetic beam, which is plotted in Figure 2.7. (It will be evident that all these curves are basically the negative lobe of an absorption characteristic of the type shown in Figure 2.2, replotted in the first quadrant for simplicity.) The main effect of the velocity spread therefore is to decrease the maximum value of the gain characteristic. This is illustrated in Figure 2.8, where the maxima of the curves of Figure 2.5 are plotted as a
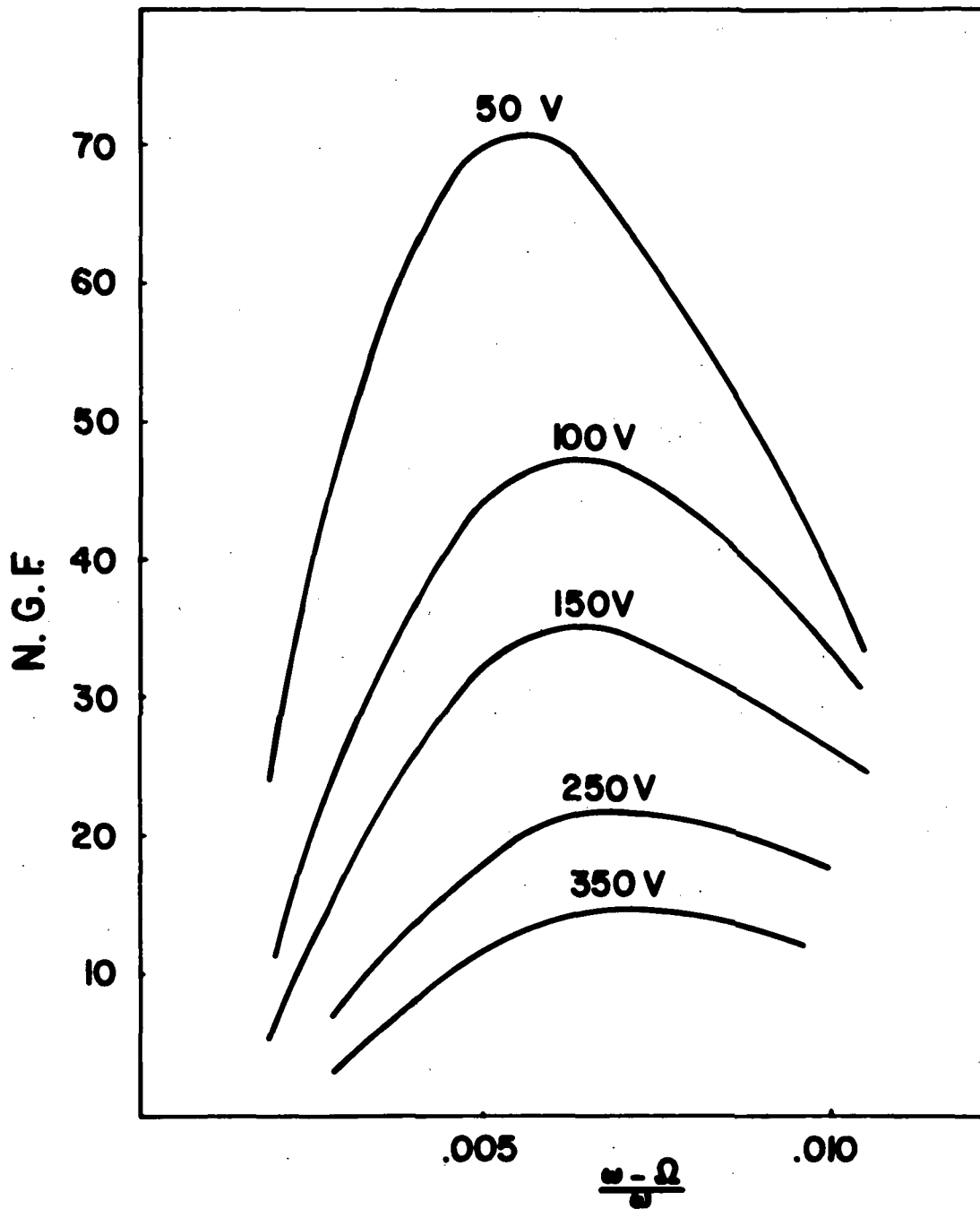
Figure 2.5.- Normalized gain function for an axial-velocity range corresponding to energies from zero to some finite value, which is the parameter. The lower limit of the energy range actually contributing to gain is 15 eV. Implicit parameters are $\lambda/\lambda_c=0.693$ and $V_o=12$ kV.

Figure 2.6.- Normalized gain function for a fixed axial-velocity range corresponding to energies from 0-100 eV. The parameter is the lower limit of the energy range actually contributing to r.f. gain. Implicit parameters are $\lambda/\lambda_c = 0.693$ and $V_o = 12$ kV.
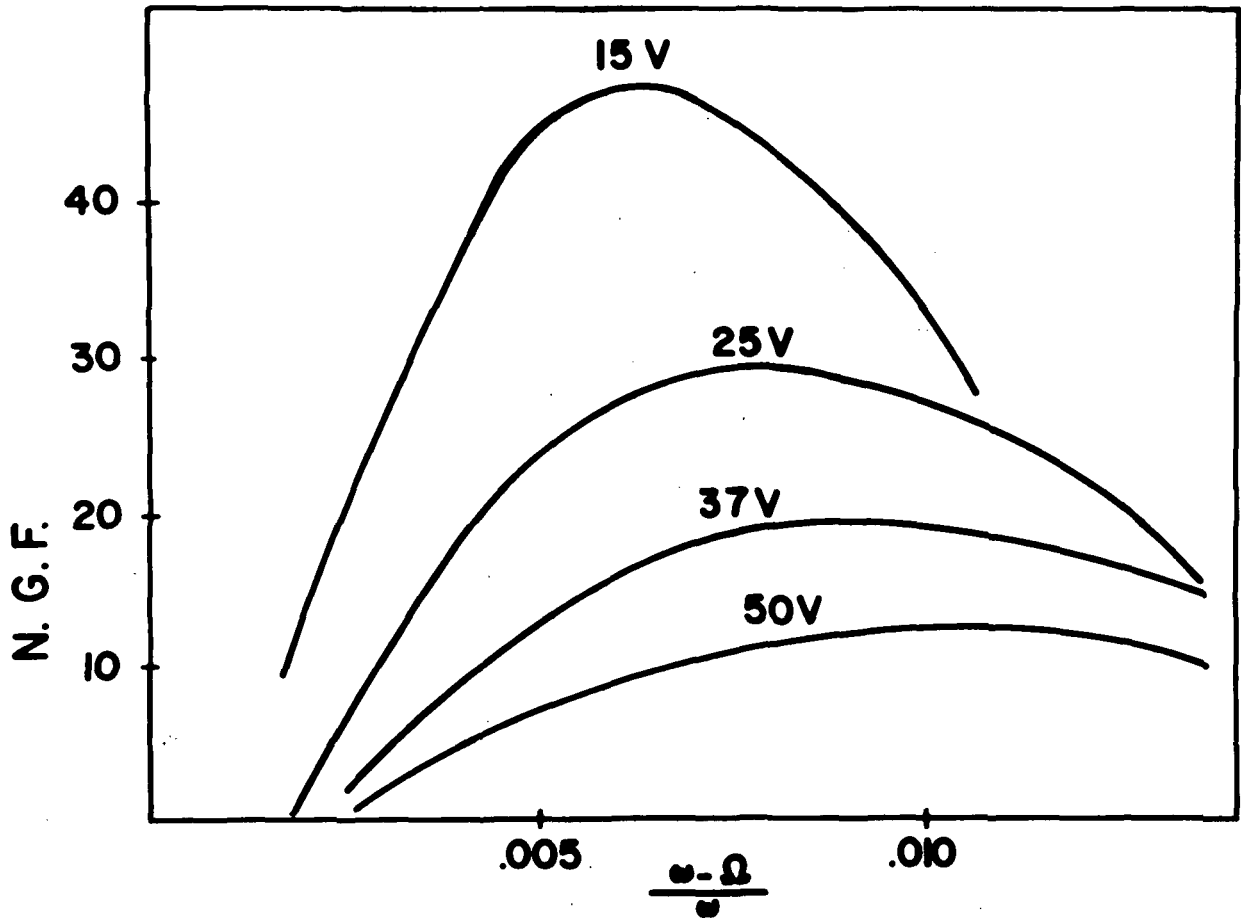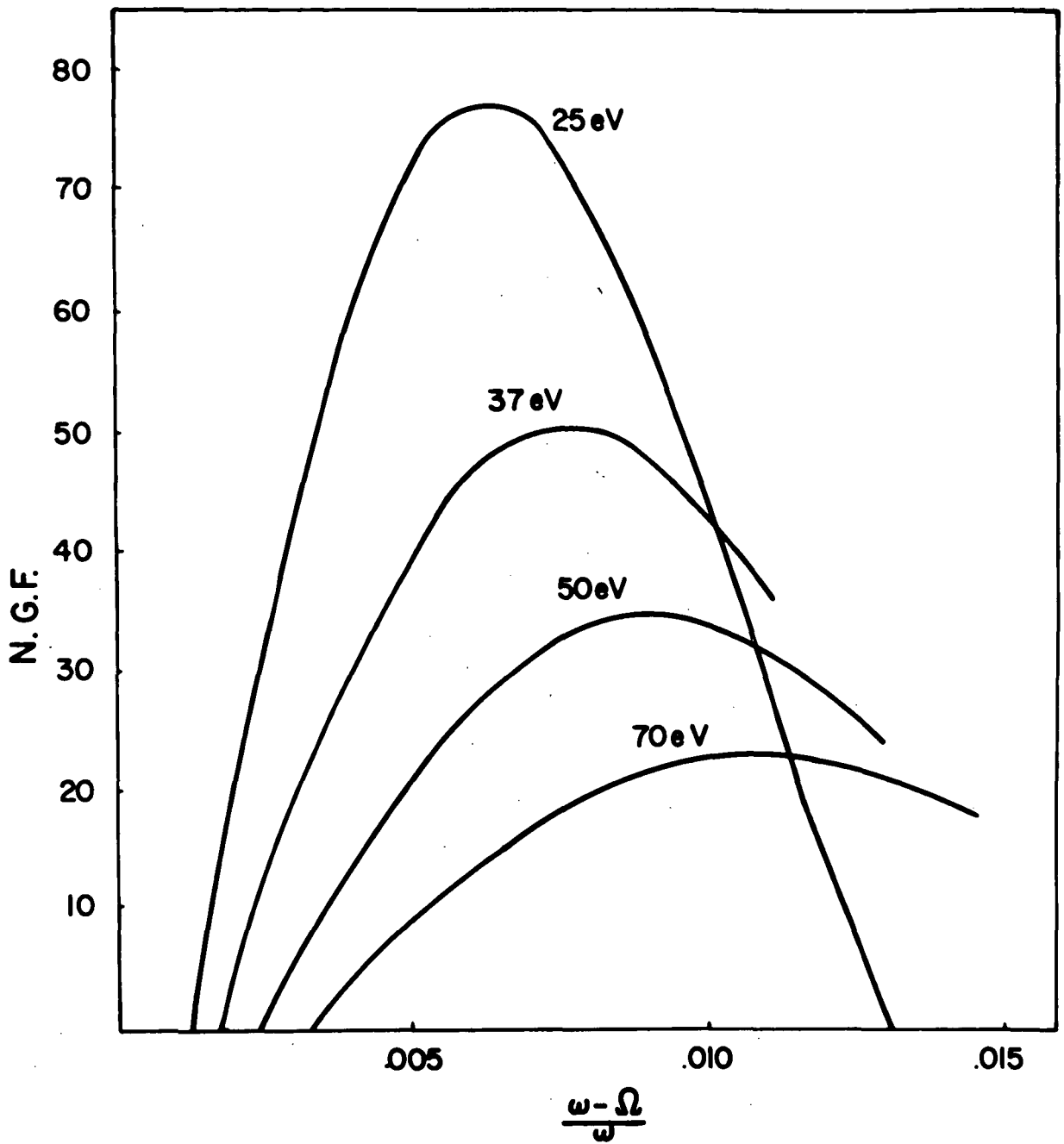
Figure 2.7.- Normalized gain function corresponding to a 12 kV monoenergetic beam with $\lambda/\lambda_c = 0.693$. The parameter is the axial energy.

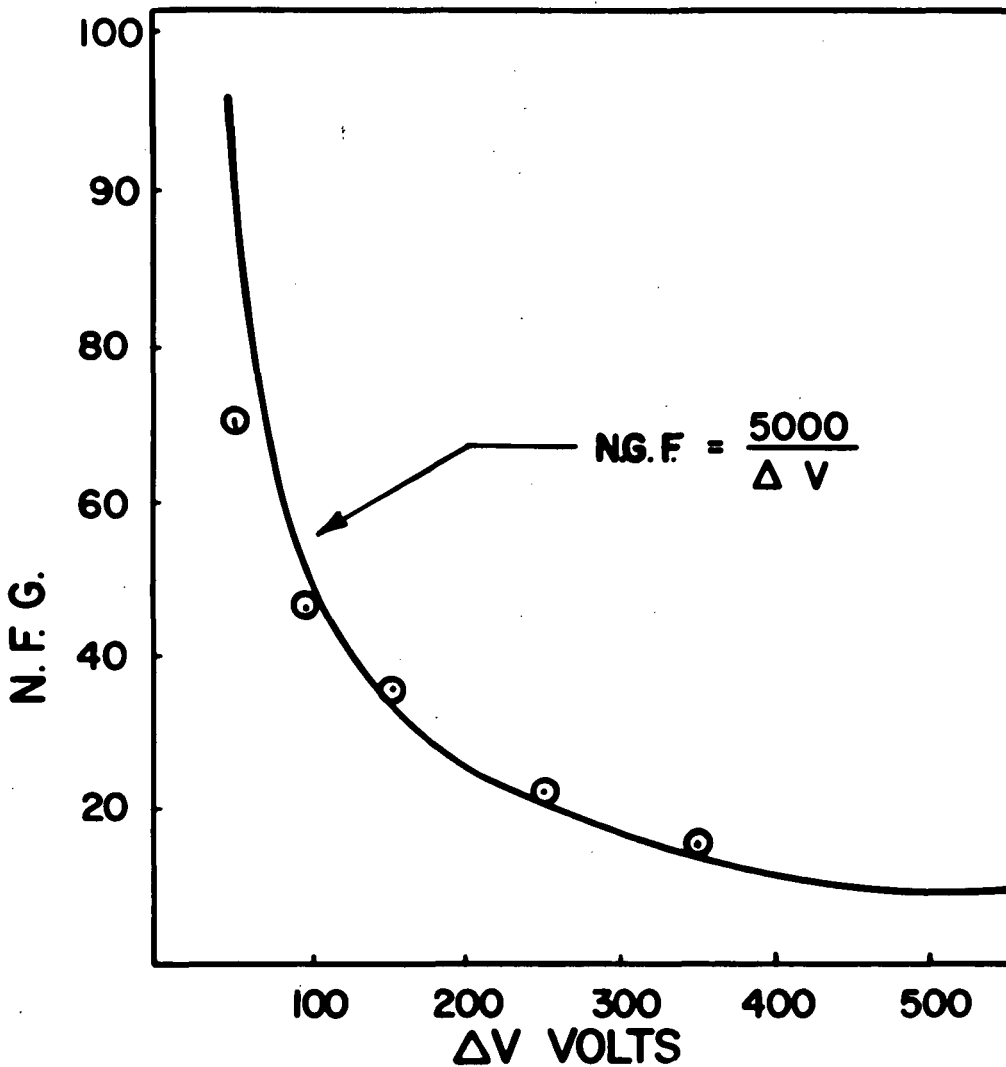Figure 2.8.- The maximum value of the normalized gain function for a 12 kV beam, with $\lambda/\lambda_c = 0.693$, plotted as a function of the axial energy spread, $0-\Delta V$. The energy range actually contributing to gain extends from 15 V to $\Delta V$. The points are derived from Figure 2.5, and they are closely approximated by the line N.G.F. = 5000/$\Delta V$.

function of the velocity spread. In fact, the calculated points can be fitted with surprising accuracy by a very simple curve, N.G.F. = 5000/($\Delta V$).

The mechanism by which very slow electrons are excluded has not been analyzed in detail. Such an analysis would involve a tedious solution of Poisson's equation for the potential within an ensemble of electrons spiraling in a strong confining magnetic field. However, Pierce (Ref. 21) has given an expression for the space-charge-limited current in a rectilinear electron beam confined by an infinite magnetic field, in terms of the potential at the beam edge, $V_o$. If in Pierce's expression $V_o$ = 15 volts, is assumed, then the limiting current is of the order of 2mA. As the operating current of the experimental tubes ranged anywhere from 1mA to 10mA or more, it seems reasonable to assume that space charge forces become significant for electrons with axial energies near 15eV.

Because the slowest electrons also produce the greatest gain, the fact that their exclusion appears to be inherent in the device constitutes an important limitation.

The dependence of the gain function on the transverse energy, i.e., the beam voltage, is linear for the mono-energetic beam, and the same can be expected to be true for a beam with finite velocity spread, from simple superposition. An experimental test of this assumption is difficult, however, because the velocity spread cannot be monitored accurately.

From Figure 2.8, it is evident that the gain decreases as the width of the axial velocity range increases. A fixed lower limit of the r.f. interaction range, such as in Figure 2.5, corresponds to the situation most likely to occur with an actual device. For this case, the maximum gain decreases as $1/\Delta V$. On the other hand, $\Delta V$ generally is proportional to the total beam energy, $V_o$, and it is reasonable to assume that the calculated gain increases linearly with $V_o$. Thus we expect that the actual gain will remain approximately constant as $V_o$ is increased because $\Delta V$ increases right along with it. The r.f. power level, on the other hand, is likely to increase as the d.c. beam power goes up. An optimum beam voltage therefore cannot be derived from the small-signal gain function, and the operating voltage used in a practical device instead must be set on the basis of the desired r.f. power level, given an expected value of efficiency.

2.4  Design of the Interaction Region

As the very rationale of periodic-beam devices implies their ability to utilize smooth, mechanically uncomplicated wave-guiding structures, the design of the interaction region is rather straightforward. In keeping with the emphasis of this report, we shall consider only standing-wave interaction.

The problem of designing a good resonator consists of selecting a geometry that will place a beam of given diameter into a region of transverse electric field possessing maximum

axial and transverse uniformity over the beam volume. A Cuccia coupler, i.e., a pair of capacitor plates forming part of a lumped-constant resonant circuit, offers a good solution at frequencies below about 1 GHz. At microwave frequencies, such a coupler can be approximated by a half-wavelength resonant section of waveguide. The axial field uniformity will depend on the guide wavelength where:

$$\lambda_g = \frac{\lambda}{\sqrt{1 - \lambda^2/\lambda_c^2}}$$

and clearly $\lambda_g$, and the field uniformity over a gain axial length, will increase as the waveguide cutoff is approached.

An extension of the resonator to multiples of a half-wavelength appears to be reasonable in view of the basic identity of traveling- and standing-wave interaction. (An analogous approach has long bean used in linear-beam extended-interaction klystrons.) However, experimental cavities longer than a half wavelength produced poor results (no observable gain) in the author's laboratory, although Bott's tube (Ref. 4) successfully had used a multiple-wavelength resonator. In any case, this discussion will be confined to simple half-wavelength resonators.

An upper limit on $\lambda_g$ is imposed, both by the difficulty of coupling to a waveguide resonator very close to waveguide cutoff, and by the requirement that the axial magnetic field must be uniform to about one part in 1000 over the interaction length.

This second constraint becomes unimportant, however, at wave-lengths of 3mm or less, because for the required field strengths, the cost of typical magnet systems is not dominated by the necessary interaction lengths. The requirement of field uniformity does impose an economic constraint at X-band, however, where the cost of the electromagnet used with an experimental device goes up rapidly with the working volume.

Two resonator modes mainly are of interest here. First, the TE(101) rectangular mode is the lowest-order resonance of a simple rectangular enclosure. Both Chow and Pantell (Ref. 2) and Schriever and Johnson (Ref. 3) successfully used simple dominant-mode rectangular waveguide in their spiraling-beam devices, in a non-resonant configuration. However, the TE(011) cylindrical mode has a larger Q and it also provides a bigger volume to accommodate the beam. Unfortunately, this mode is degenerate with the TM(111) mode, and the latter may have to be suppressed. One observes that the TE(011) is the lowest-order member of the family of "barrel modes", TE(n, 1, 1), any of which could furnish a region of transverse electric field for interaction with the beam. However, the azimuthal polarization associated with all but the TE(011) mode can lead to coupling problems. In addition, the TE(011) has by far the greatest Q among the TE(n, 1, 1) family. In normalized form, this can be written as (Ref. 22):

$$Q \frac{\delta_s}{\lambda_o} \frac{\left(1 - \frac{1}{\left(p_{nl}^1\right)^2}\right)\left(p_{nl}^1\right)^2 + \left(\frac{\pi a}{d}\right)^2 {}^{3/2}}{2\pi\left[\left(p_{nl}^1\right)^2 + \frac{2a}{d}\left(\frac{\pi a}{d}\right)^2 + \left(1 - \frac{2a}{d}\right)\left(\frac{n\pi a}{p_{nl}^1 d}\right)^2\right]} \qquad (2.16)$$

for a circular TE(n, 1, 1) cavity of radius a and length d,

where $\delta_s$ is the skin depth and $\lambda_o$ the free-space wavelength.
The $p_{nl}^1$ are the zeros of the appropriate Bessel function, i.e.,
$p_{ol}^1$ = 3.832, $p_{11}^1$ = 1.841, etc.  In Table 2.1, some numerical

values are given for the case where $\lambda/\lambda_c$ = 0.95, where $\lambda_c$ is

the cutoff wavelength of the $TE_{n,1}$ mode in cylindrical guide of

radius a.

TABLE 2.1.- NORMALIZED QUALITY FACTORS FOR THE
$TE_{n,11}$ MODES, ASSUMING $\lambda/\lambda_c$ = 0.95

| n | $Q \frac{\delta_s}{\lambda}$ |
|---|---|
| 0 | 0.66 |
| 1 | 0.23 |
| 2 | 0.30 |
| 3 | 0.35 |
| 4 | 0.38 |
| 5 | 0.42 |

The cavity Q, by itself, provides only a rather vague yard-stick for cavity design, however. A more useful figure of merit for cavity performance can be derived from the expression for the r.f. power, P, given up by the beam, Eq. (2.3). It will be noted that the cavity characteristics appear only through the term $E_o^2/k_{11}^2$. In order for oscillations to start, the power derived from the beam must equal or exceed the ohmic losses $W_L$ of the cavity plus the external load:

$$P = W_L$$

From Eq. (2.3), the start-oscillation current will then be inversely proportional to a quantity having the dimensions of an impedance:

$$\left(I_{start}\right)^{-1} \propto \frac{E_o^2}{k_{11}^2 W_L} \equiv K \tag{2.17}$$

This will be termed the interaction impedance. As the ohmic loss can be written $W_L = \frac{\omega U}{Q}$, the interaction impedance becomes:

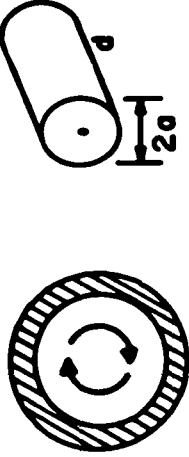$$K = \frac{E_o^2 Q}{k_{11}^2 \omega U} \quad \text{(ohms)} \tag{2.18}$$

where U is the energy stored in the cavity. If only internal losses are considered, $Q = Q_o$, and $K \equiv K_o$ then depends entirely on the cavity geometry. On the other hand, external loading is

easily accounted for by setting $Q = Q_L$, the loaded Q. Expressions for $Q_O$ and $K_O$ have been derived for both the TE(101, rectangular) and the TE(011, cylindrical) resonators, and these are given in Table 2.2. These expressions have been derived from equations given in the literature (Ref. 13). Both $Q_O$ and $K_O$ are normalized to $\delta_s/\lambda$ where $\delta_s$ is the skindepth and $\lambda$ is the free-space wavelength. In formulating the expressions for $K_O$, the peak value of electric field was assumed to hold over the entire beam cross-section, neglecting any small correction factors that would arise from averaging. For the beams used here, this approximation produces a maximum error in $K_O$ of about five percent.

Figure 2.9 gives the plots of $K_O$ and $Q_O$ vs $\lambda/\lambda_c$. Clearly, despite its relatively low $Q_O$, the rectangular TE(101) mode has about double the interaction impedance of the circular mode, and it was selected for this reason in the X-band prototype devices, as well as for the first model of the 94 GHz device. However, the somewhat greater physical size of the $TE_{011}$ cavity is attractive at mm wavelengths, and so this mode was chosen for the second 94-GHz tube.

The design parameters for some resonators that were used in actual working devices, are listed in Table 2.3. Resonators Nos. 1-3 were coupled magnetically to a feeder waveguide via a round aperture in the narrow wall of the guide. Resonator No. 4 had its WR 10 feeder guide on the beam axis, and the coupling took place via a short section (1.2 mm) of the same waveguide

TABLE 2.2. – MODE CHARACTERISTICS FOR TE$_{(101)}$ AND TE$_{(011)}$ MODES

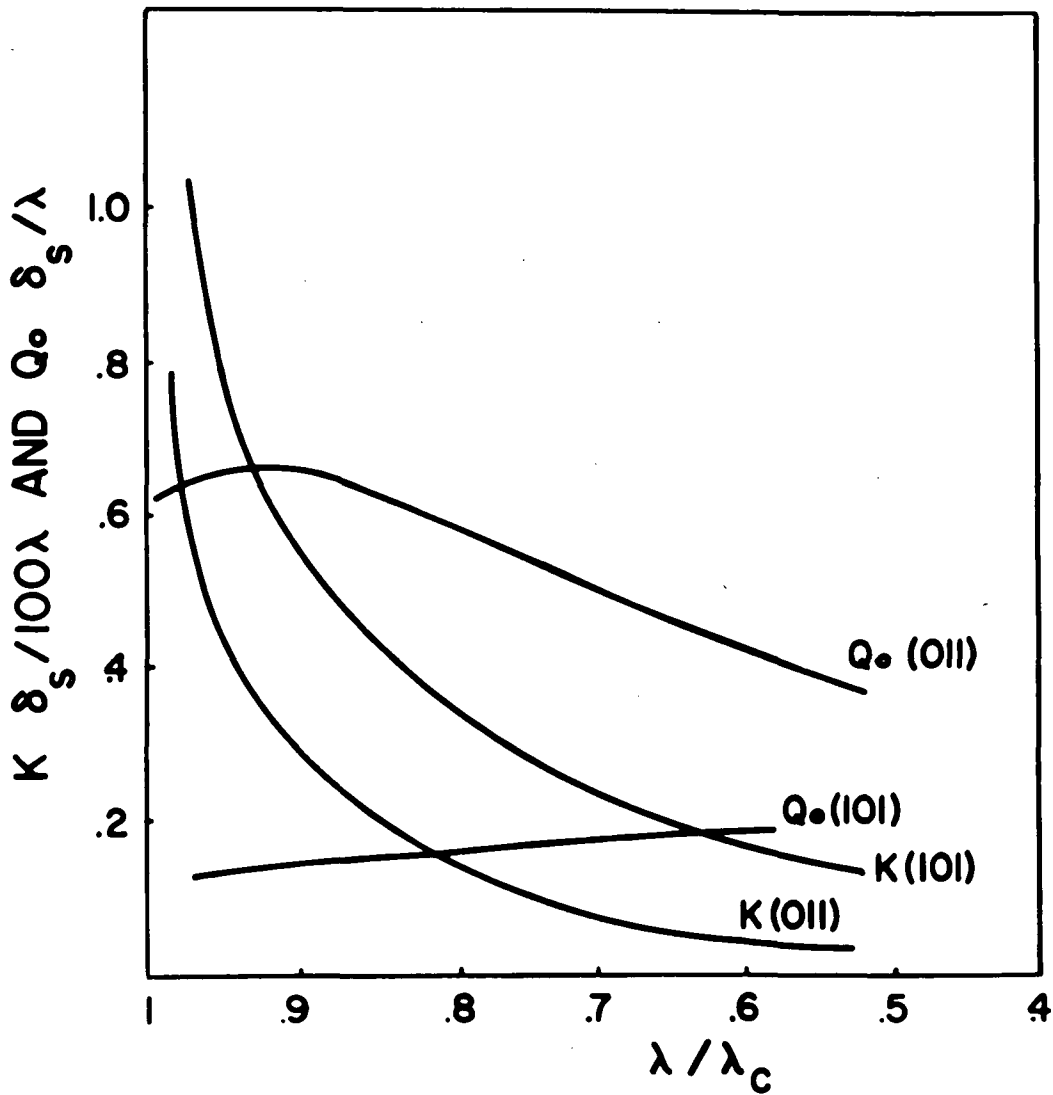| MODE | ELECTRIC FIELD CONFIGURATION | EXPRESSIONS FOR Q$_o$ AND K |
|---|---|---|
| TE$_{(101)}$$^{rect.}$ |  $E_y = E_o \sin\frac{\pi x}{a} \sin\frac{\pi z}{d}$ <br><br> $E_x = E_z = 0$ | WITH $b = \frac{1}{2}a$, $\frac{\lambda}{\lambda_c} = x$, $\frac{\lambda}{d} = y$, <br><br> $\frac{\delta_s}{\lambda} Q_o = \frac{1}{4} \frac{(1+y^2)^{3/2}}{2+y^3} \frac{\sqrt{1-x^2}}{x}$ <br><br> $K\frac{\delta_s}{\lambda} = \frac{4}{\pi^3}\sqrt{\frac{\mu}{\epsilon}}\sqrt{1-x^2} \cdot \frac{(1+y^2)^{3/2}}{y^2(2+y^2+y^3)}$ |
| TE$_{(011)}$$^{cyl.}$ |  $E_\phi = A\, j_o'(k_c r)\cos\frac{\pi z}{L}$ <br><br> $E_\gamma = E_z = 0$ | WITH $\frac{\lambda}{\lambda_c} = x$, $\frac{a}{d} = 1.22$, <br><br> $Q_o\frac{\delta_s}{\lambda} = \frac{1}{2\pi} \cdot \frac{[14.68 + (\frac{\pi a}{d})^2]^{3/2}}{[14.68 + \frac{\pi a}{d}(\frac{\pi a}{d})^2]} \frac{\sqrt{1-x^2}}{x}$ <br><br> $K\frac{\delta_s}{\lambda} = 3.467\left(\frac{x}{\sqrt{1-x^2}}\right)\frac{[14.68 + (\frac{\pi a}{d})^2]^{3/2}}{[14.68 + \frac{2a}{d}(\frac{\pi a}{d})^2]}$ |

Figure 2.9.- Normalized interaction impedance and quality factor for cavity resonators in the TE(101) rectangular and the TE(011) circular modes, plotted vs $\lambda/\lambda_c$.

TABLE 2.3.- DESIGN PARAMETERS FOR SOME EXPERIMENTAL RECTANGULAR CAVITIES

| No. | Dimensions | Nominal $f_o$ | $\lambda/\lambda_c$ | $Q_o$ | $Q_L$ | $K$ | Coupling Aperture |
|---|---|---|---|---|---|---|---|
| 1 | a=2.286 cm<br>b=1.016 cm<br>d=4.196 cm | 9.6 GHz<br>$TE_{102}$<br>rect. | 0.70 | 9600(theo.)<br>4000(meas.) | | $1.26 \times 10^6 \, \Omega$ | Circular<br>0.794 cm dia.<br>x 0.064 cm thick<br>VSWR = 1 |
| 2 | a=2.286 cm<br>b=1.016 cm<br>d=2.141 cm | 9.6 GHz<br>$TE_{101}$<br>rect. | 0.70 | 7800(theo.)<br>3600(meas.) | 650 | $1.14 \times 10^6 \, \Omega$ | Circular,<br>0.635 cm dia.<br>x 0.064 cm thick<br>VSWR = 5.6<br>(overcoupled) |
| 3 | a=1.788 cm<br>b=0.635 cm<br>d=3.134 cm | 9.6 GHz<br>$TE_{101}$ | 0.88 | 6000(theo.)<br>3200(meas.) | | $1.88 \times 10^6 \, \Omega$ | Circular,<br>0.561 cm dia.<br>x 0.064 cm thick<br>VSWR = 1 |
| 4 | a=0.254 cm<br>b=0.127 cm<br>d=2.459 cm | 94 GHz<br>$TE_{1,0,12}$<br>rect. | 0.63 | 4000(theo.)<br>$\approx$1400(meas.) | | $0.40 \times 10^6 \, \Omega$ | Square,<br>$(0.127cm)^2$<br>x 0.117 cm thick |

rotated 90° about the axis, i.e,, a section below cutoff for
the dominant mode.

In the final experiment at 94 GHz, a circular TE(011)
resonator was used, with dimensions 4.1-mm diameter x 5.3 mm
length.  This was coupled to a WR-10 feeder waveguide through
a 0.94 mm diameter round iris in the 0.01-mm thick sidewall,
which made the cavity undercoupled with VSWR $\simeq$ 3.5 at $f_o$ = 92.59
GHz.  The theoretical $Q_o$ was 5000, and the measured $Q_L$ was
estimated at better than 1300.  The calculated interaction
impedance is K = 320 k$\Omega$.

## 2.5  Summary

In this section, we have investigated the small-signal
electronic gain arising from the interaction of a spiraling
electron beam with either a traveling-wave or a standing-wave
electromagnetic field.  It was found that the basic interaction
is one between the spiraling electrons and a traveling wave,
even in the standing-wave environment.  Device operation close
to waveguide cutoff results in the greatest amount of electronic
gain, and in this range the dominant bunching mechanism is due
to the relativistic mass change of the electrons as they are
accelerated or retarded by the electric field component of the
traveling wave.  D.C. space-charge forces appear to prevent
axially slow-moving electrons from participating in the r.f.
interaction, and the faster electrons are spread out over a
finite energy range.  Both these factors are basic device

limitations which reduce the electronic gain to a small fraction of that attainable with an ideal mono-energetic beam of near-zero axial drift velocity. There exists a threshold value for the beam voltage below which there is no electronic gain. However, an optimum value of $V_o$ cannot be derived from the small-signal gain characteristics.

The geometry of the interaction region can be optimized in terms of an interaction impedance that derives from the gain equation. Design curves and examples are given for two typical resonator geometries.

# 3. AN EXPERIMENTAL SPIRALING BEAM

In this section, we shall discuss some techniques which were used to generate spiraling electron beams, together with the characteristics of typical beams. It should be mentioned at the outset that the spiraling-beam guns designed in the course of this program were very simple. However, the importance of beam quality, in terms of velocity spread, did emerge very clearly, and any future work on these devices should concern itself first and foremost with the development of an electron gun capable of producing a nearly monoenergetic spiraling beam.

## 3.1 Generation of a Spiraling Electron Beam

The discussion in the last section emphasized that the dominant requirement in a spiraling beam device is, simply, that the electrons should have as narrow as possible an energy spectrum, with practically all the energy being transverse. The ideal case then is a delta function velocity distribution. In a practical beam, the electron energies will be spread out over a finite range, however, and the width of this range is closely tied to the method of generating the beam.

The approach to beam design used in this project was essentially adopted from some previous, successful experiments made elsewhere (Refs. 4,9). A sketch of the basic scheme is shown in Figure 3.1. One starts with a thin (1-3 mm dia.) rectilinear beam launched from a diode or triode gun, immersed in a magnetic field of 3 to 4 times the theoretical minimum
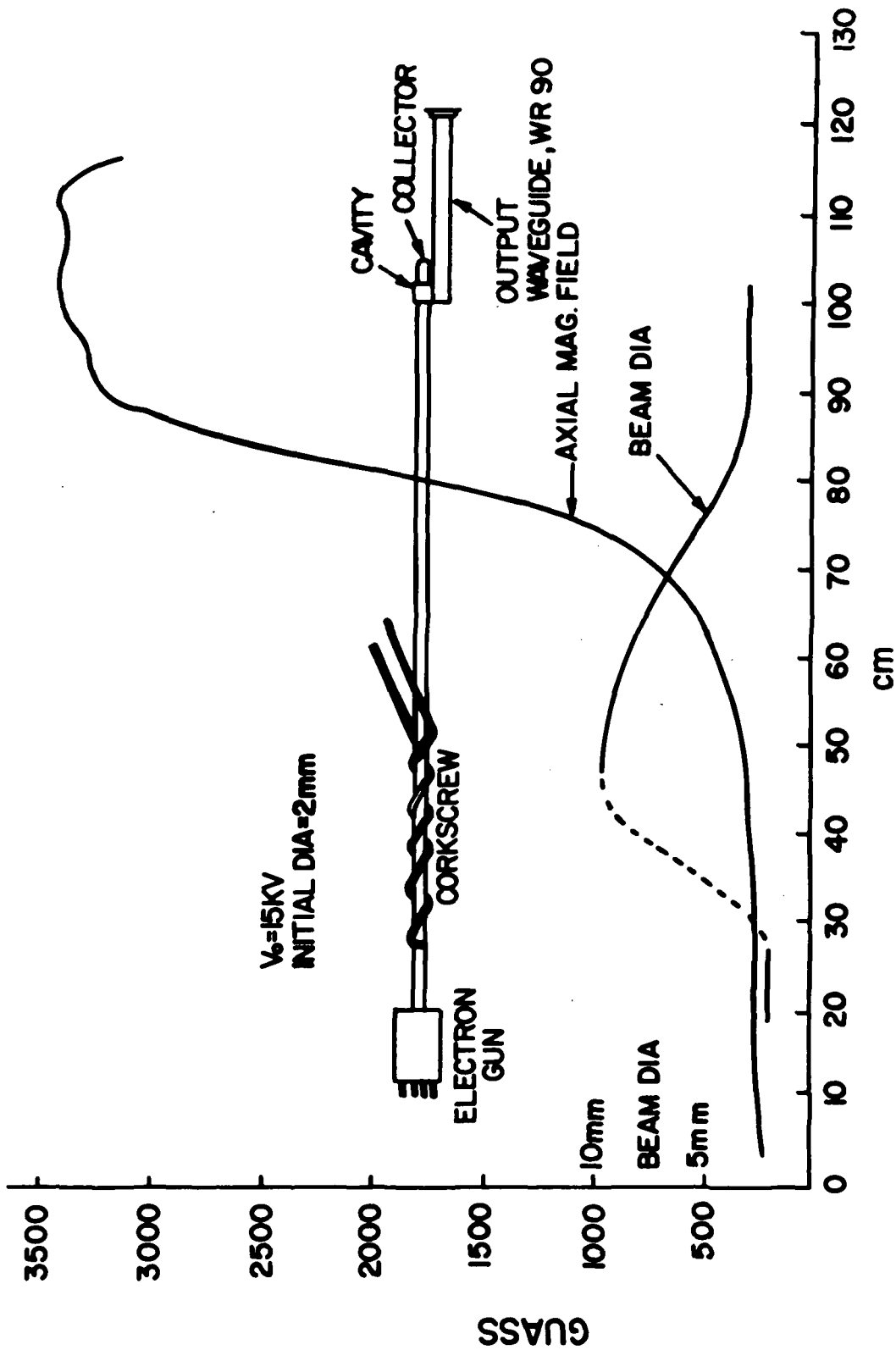
Figure 3.1.- X-band prototype device and calculated beam profile, shown to scale with the measured axial magnetic field.

required to focus the beam stably. The beam then travels through a drift region where a magnetic corkscrew (Ref. 23) sets up a space-periodic, transverse, magnetic field component with a strength of about 1% of the axial field intensity. The corkscrew action causes a momentum conversion on the beam, adiabatically changing as much as 10% of its (initially axial) energy into rotational energy. A mildly spiraling beam results, where the spiral itself remains fixed in position, much like a snaking garden hose through which electrons are running. (This was verified photographically in a special beam tester.) Further momentum conversion takes place as the beam drifts into a region of increasing magnetic field, i.e., up a magnetic ramp, to the point where practically all its energy is transverse. The beam at this point has become an ensemble of energetic electrons tightly spiraling about individual magnetic flux lines as guiding centers, and drifting axially at a relatively slow rate.

Figure 3.1 depicts an X-band device to scale in the measured axial magnetic field profile, together with the calculated beam diameter. The field strength is plotted as a function of distance along the axis.

The magnetic-field profile was generated from a long thin solenoid (laser coil, 10-cm bore, 76-cm long) for the low-field region, and a set of four short, butted solenoids (plasma coils, 10-cm bore, 10-cm long) for the high field. All coils were water-cooled. The plasma coils could not be positioned at the

Helmholtz spacing because of the width added by their cooling pancakes, and this made it physically impossible to produce a perfectly smooth high-field plateau. These coils were later replaced by a regular Helmholtz system consisting of two solenoids (11.5-cm bore), with each solenoid made up of two halves that each were spaced at the Helmholtz distance by centrally located cooling pancakes.

While the earlier ripples in the high-field plateau did not seem to produce any observable effect on the r.f. interaction directly, they may have caused some charge trapping which then resulted in ion oscillations. For example, with a 15-kV beam from a 2-mm dia. cathode, a 100-kHz oscillation appeared on the collector current pulse with an amplitude of about 5% of the total pulse height. At a pressure of $2.5 \times 10^{-6}$ Torr, this instability would appear about 15 - 20 μsec, after the start of the pulse, and would lose coherence after another 20 μsec, becoming essentially noise at this point. The time of onset showed a clear dependence on the pressure, when the latter was allowed to rise by turning off the getter pump. The identical instability also appeared on the r.f. pulse. No such instability was observed after the Helmholtz system had been installed.

The use of iron in the magnetic circuit was generally avoided in order to retain maximum flexibility in adjusting the ramp geometry. However, soft iron cladding was eventually used around the low-field solenoid in order to shield it from the

high field, which otherwise tended to upset the axial-field uniformity along the low-field plateau. The corkscrew design has been discussed in a previous report (Ref. 17) and will only be sketched here. The corkscrew typically consisted of a section of quadrufilar helix that was found from #14 enameled copper wire, with a constant pitch given by:

$$p_C = \frac{2\pi u_o m}{eB_o} \tag{3.1}$$

where $u_o$ and $B_o$ are the axial beam velocity and the axial magnetic field in the gun region, respectively. The winding was done by hand, with the aid of a pencil sketch of the developed helix that was rolled as a template around the 16-mm dia. drift tube. The length of the corkscrew section was determined by the axial distance over which the low-field plateau remained uniform within 1%, typically, about 25 cm. The corkscrew was driven with direct current of 3A - 10A magnitude. A typical example of corkscrew action is shown in Figure 3.2.

When the low field is tuned to cyclotron resonance, the corkscrew action produces a dip in the collector current. Both the height and the width of this dip increase as the corkscrew current is raised.

The electron guns used in this work were simple Pierce designs using 1-, 2-, or 3-mm dia. dispenser-type cathodes. A first anode was used to control the beam current, and a second
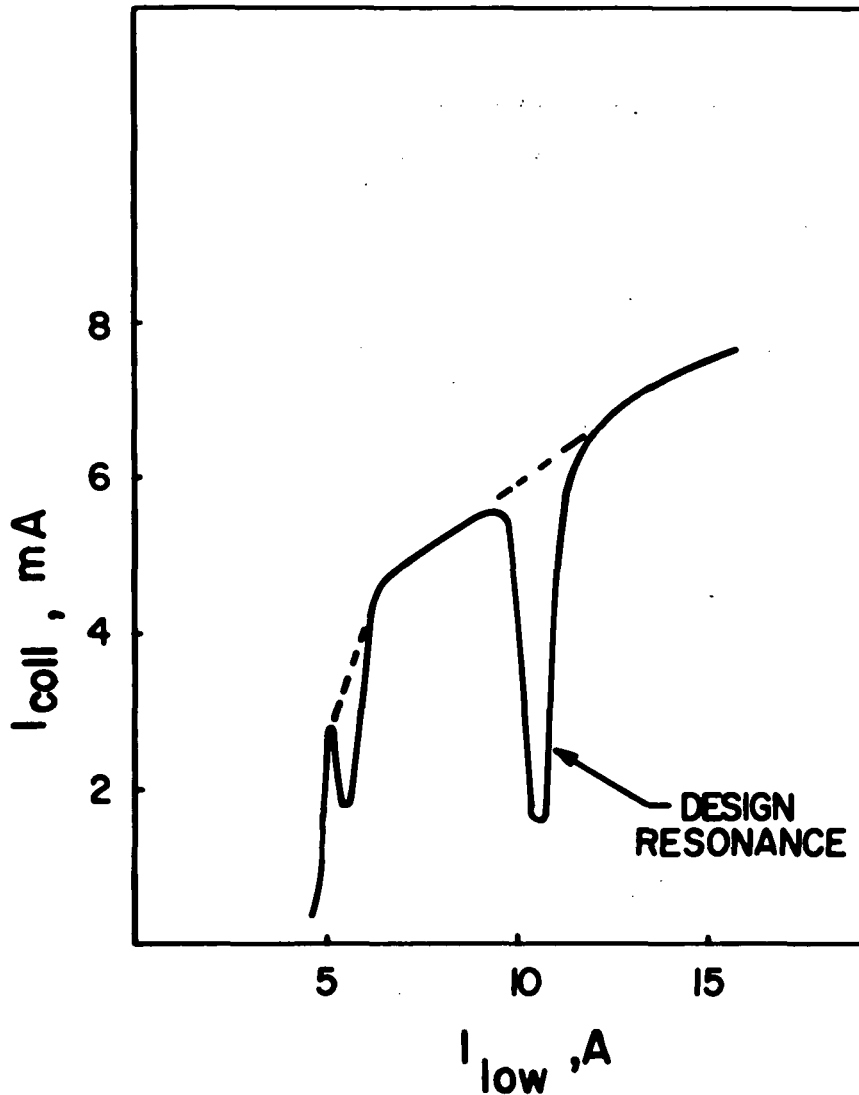
Figure 3.2.- Typical focusing characteristic, showing the effect
of the corkscrew action on the collector current.
The dashed line indicates the simple focusing action
of the low field, ($I_{cork}=0$) resulting in increased
transmission as the control-anode interception is
reduced. The solid line shows the corkscrew action
superimposed, with $I_{cork}=5.5A$. Design parameters
are $V_o=12$ kV, 1 mm dia. cathode, corkscrew pitch
= 7 cm (quadrufilar), dia. 1.6 cm, length 25 cm, low
field 32.1 Gauss/A, high field 3500 Gauss.

anode served to accelerate the beam up to the operating potential. Beam current sometimes also was controlled by temperature-limiting the cathode. The anodes typically were flat molybdenum or Cu-Ni disks, 2.22 cm dia. x 0.13 cm thick, with a small opening for beam passage. They were held either by a three-rod ceramic frame or by a set of boron-nitride bushings. The gun structure was built up on a stainless-steel vacuum flange which made it easily demountable for cathode replacement or minor design changes. All the guns contained identical 10-W heaters. The perveance was of the order of 0.01 micro perv. Further details about beam voltages and currents are given in connection with the experimental results.

Because the corkscrew action produces a finite amount of velocity spread on the beam, and because the magnetic ramp amplifies this spread linearly, the electrons are distributed over a wide energy range by the time they reach the top of the ramp. Inevitably some electrons will exceed the point of 100% energy conversion and will be mirrored back towards the gun, while others may not reach the range of axial velocity that allows them to interact with the r.f. fields. As a result, the beam is used very inefficiently, as typically only 30% or less of the current *emitted from the cathode actually passes through the interaction* region, with the rest being mirrored back. The r.f. conversion efficiencies are quoted here in terms of the collector current, and these numbers would be smaller by a factor of three or more

if the cathode current were used as a basis for calculating the efficiency.

## 3.2 Energy Distribution

When the importance of the corkscrew-generated velocity spread became apparent during this work, a retarding-field analyzer was built and set up to measure the energy distribution of a typical beam (Ref. 24).

Briefly, these measurements indicated that in the absence of space-charge effects, the corkscrew will generate a relatively narrow, near-rectangular axial energy distribution when the axial magnetic field is tuned to near cyclotron resonance. The normalized width of this distribution is nearly independent of the degree of energy conversion, in agreement with the theory, and the mean transverse (converted) energy varies as the square of the corkscrew current. The magnetic ramp amplifies both the mean transverse energy and the energy spread linearly, as expected from the assumed adiabatic conversion.

Actually, the magnetic ramp itself can also be used to analyze the axial energy spread produced by the magnetic cork-screw, if a simple conversion relation is used to transform the magnetic ramp data into the more familiar retarding-field analyzer form (Ref. 25). Figure 3.3 shows some axial velocity distributions for a 4-kV, 200-µA beam with an initial diameter of 1 mm, measured with the electrostatic analyzer with a constant mirror ratio $M = 8.53$. The parameter is the corkscrew current. (The mirror

ratio is defined as the ratio of the high-field to the low-field magnetic field intensities, $M = B_1/B_o$).

It should be noted that there is a one-to-one correspondence between the axial and the transverse energy distributions, because energy is conserved. Hence, a movement of the axial energy distribution towards lower energies, as $I_{cork}$ is raised, will be accompanied by a corresponding movement of the transverse distribution towards higher energies.

When the corkscrew is tuned slightly <u>above</u> cyclotron resonance, such as in Figure 3.3, the axial distribution becomes reasonably rectangular, and constant in width and it will here be approximated as such. An idealized operating situation is shown in Figure 3.4, where a fraction of the electrons are already being mirrored, while the r.f. interaction takes place over the remaining part of the energy distribution. By mirroring a part of the beam, we are thus, in effect, simulating a new beam with less current and with a narrower energy distribution, and the r.f. interaction must be analyzed in terms of this new beam. Because it proved to be very difficult to make direct measurements of this new narrow distribution, especially the part close to the origin, a simple rectangular shape continued to be the working assumption.

The width of the entire distribution can be estimated from a knowledge of the energy spread introduced by the corkscrew. From the data obtained with the retarding-field analyzer (Ref. 24), this spread was typically near 5% for guns and corkscrews of the
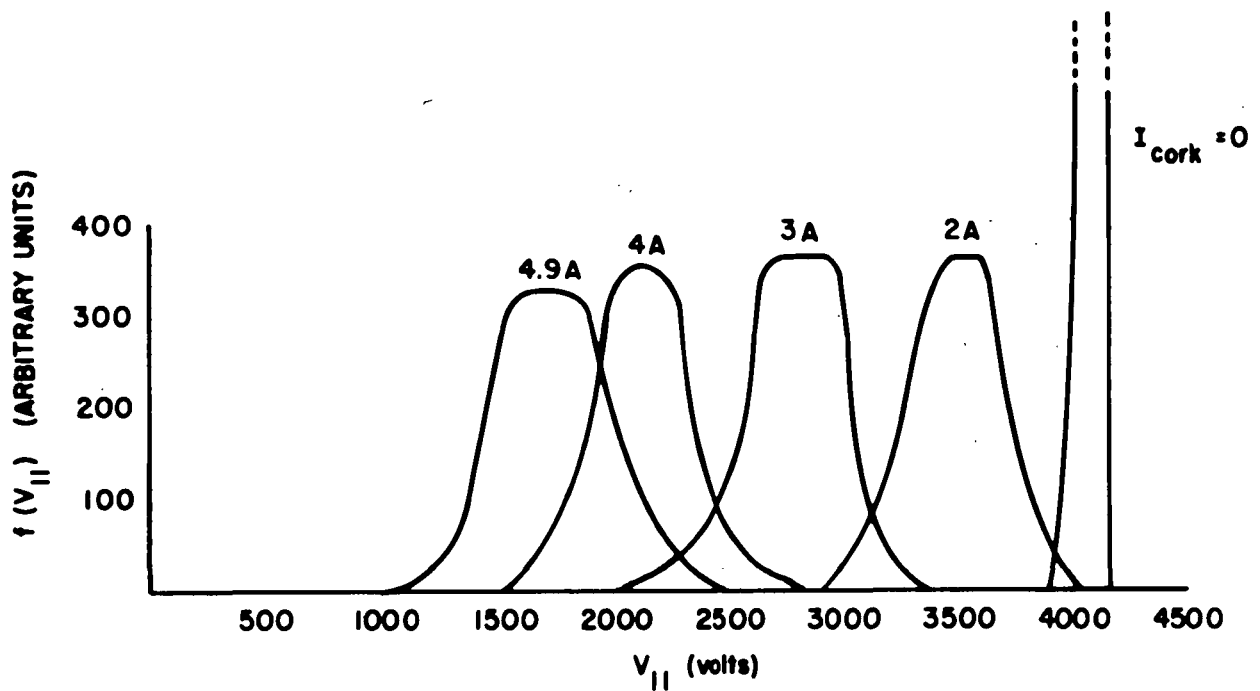
Figure 3.3.- Axial energy distribution measured on a 4 kV, 200 μA beam with initial diameter 1 mm, after passage through a quadrufilar-helix magnetic corkscrew of length 33 cm, pitch 3.33 cm, and diameter 1.6 cm. The parameter is the corkscrew current. The mirror ratio is $M = B_1/B_0 = 8.53$. The low field is adjusted to a value 3.5% above nominal cyclotron resonance.

type used here. Given a mirror ratio of about 10 for the X-band experiments, this results in an estimated overall energy spread near 50%. The magnetic-field profile used at 94 GHz had mirror ratios up to 100, corresponding to a total energy spread up to 500%, if the simple theory is followed. Actual operating conditions at X-band were such that only about one-third or less of the beam current reached the collector, with the rest being mirrored back. This would correspond roughly to a 15% spread of the effective distribution, based on the simple model of Figure 3.4.

From this model, one would also expect to see some electronic gain as soon as the collector current begins to decrease due to the mirroring action. This, in fact, is the case, and as the corkscrew current is increased from zero the observed gain first increases to a maximum and then decreases again. The exact behavior follows from the normalized (average) gain character- istics discussed in the previous section, multiplied by the number of available electrons, i.e., the collector current. A calculation of this type is performed in the following section.

In summary, while the method of generating a spiraling beam with a corkscrew-magnetic ramp combination is very simple and very flexible in laboratory applications, it is not recommended for commercial devices of this type, because of the wide energy distribution that appears to characterize it. Any further development work on periodic-beam devices certainly should place

the strongest emphasis on the design of a good beam. Conceivably,
more direct methods of generating the spiraling trajectory could
result in less velocity spread. For example, guns where the
cathode-anode geometry is tilted in the magnetic field have been
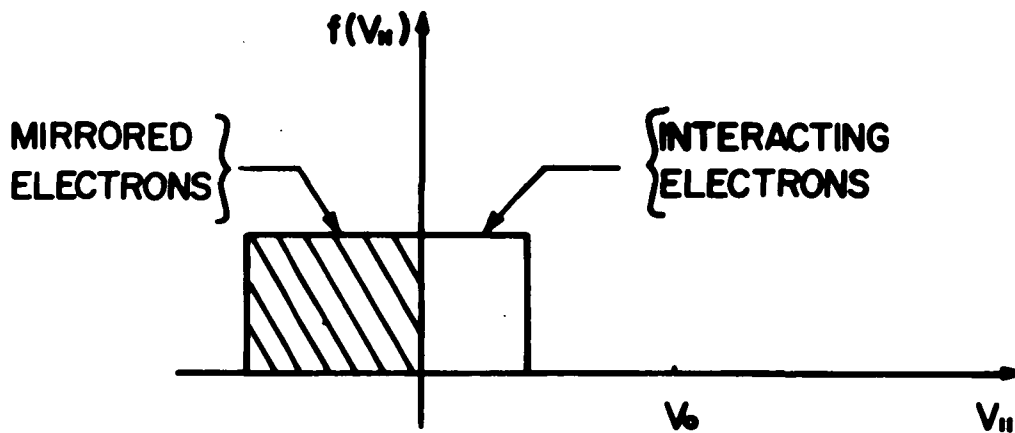used successfully by other workers (Refs. 3,10).



Figure 3.4.- Approximate model of a typical operating distri-
bution of the axial electron energies. Only a
small energy range near the mirroring point is
being utilized in the r.f. interaction.

# 4. EXPERIMENTAL TECHNIQUES AND RESULTS

In this section, we shall summarize and discuss the results of experiments made with a number of prototype spiraling-beam amplifiers, all of which were built in-house. The objectives of these experiments were, first, to verify the small-signal model, and to acquire a reasonable working knowledge of this type of device, and second, to arrive at some quantitative estimate of the practical limits on power level, efficiency, and frequency. First, the instrumentation will be described.

## 4.1 Instrumentation and Measurement Techniques

A basic sketch of a typical experimental setup has already been given in Figure 3.1, in this case, for the first X-band tube. The design parameters for the different cavity resonators used were listed in Table 2.3. In the following, we shall discuss the detailed instrumentation, a sketch of which is drawn in Figure 4.1.

The two high-field coils were each driven, somewhat marginally, by one HP6459A supply. These supplies were voltage-controlled from a common, variable, well-regulated d.c. voltage source. This method of control accomplished the necessary ganging of the supplies, while at the same time permitting vernier changes in individual current settings. The supplies were monitored individually by means of digital voltmeters connected across 0.01 ohm current-sensing resistors, and this assured accurate day-to-day duplication of high-field settings. The
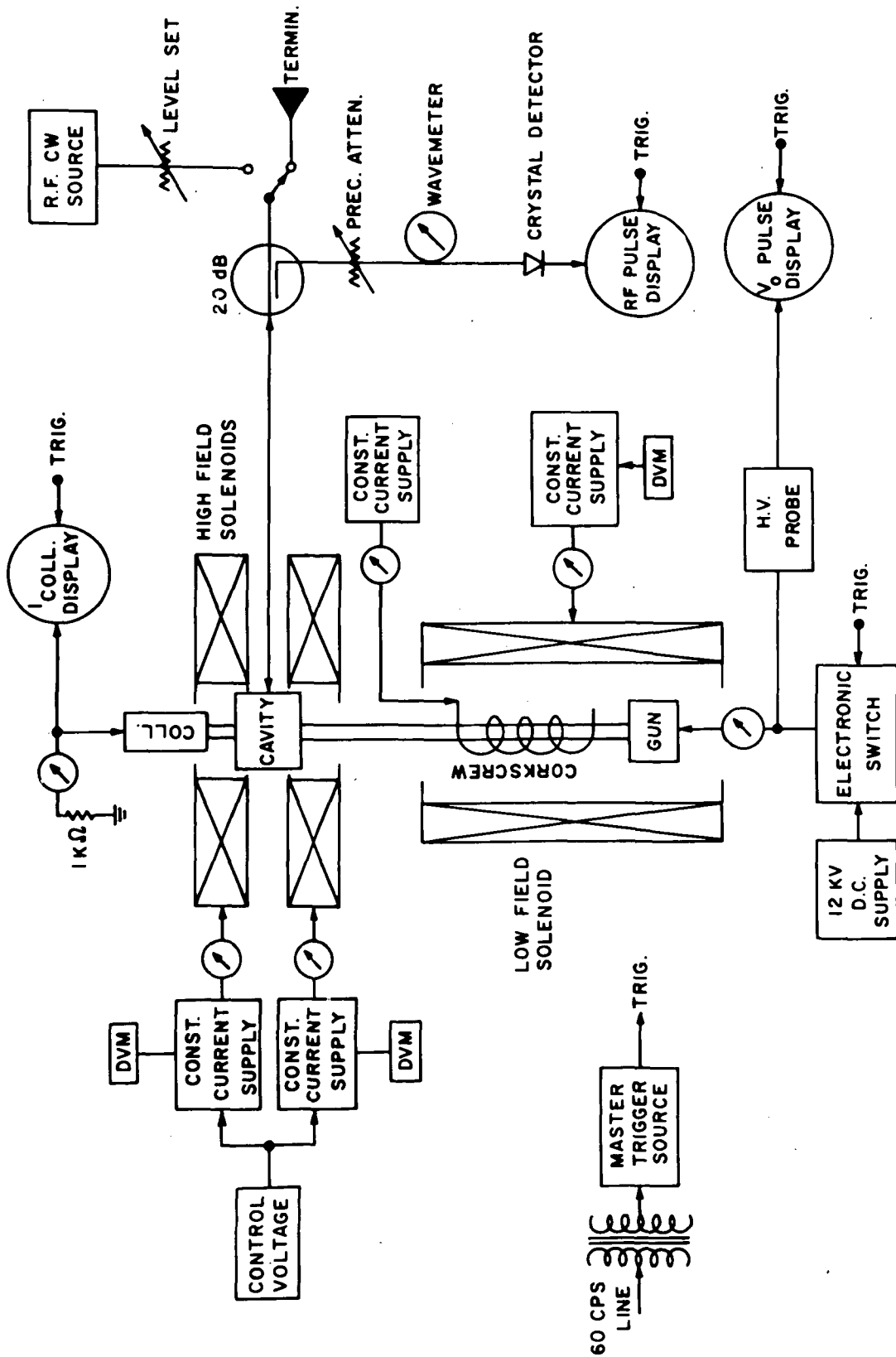
Figure 4.1.- Instrumentation for the X-band experiment

low-field solenoid also was driven from a well-regulated supply, and its current was monitored with a digital voltmeter.

In order to avoid problems of Joule heating and d.c. voltage breakdown, the tubes were operated pulsed-cathode only, with pulse lengths from 10-50 μsec at 60 pps. Line synchronization was found to be necessary in order to stabilize the oscilloscope displays, especially those of low-level r.f. signals. Both the beam voltage and the collector current were scope-monitored, while the cathode and first-anode current were metered conventionally. Where it was desirable to drive an X-Y recorder from the pulse amplitude either of the collector current or of the r.f. output signal, the pulse train was converted to a d.c. amplitude by using a boxcar integrator.

The r.f. circuitry was designed to perform the dual function of measuring r.f. gain with a probing signal fed in, or of measuring output power after self-excited oscillation had begun. The power measured used a calibrated crystal together with a precision waveguide attenuator. The gain measurement was accomplished by comparing the return loss (or VSWR) with the beam ON to that with the beam OFF. Further details will be discussed, in conjunction with the measured results.

The instrumentation used for the 94-GHz experiment was very similar to that shown in Figure 4.1. A superconducting magnet generated the high-field plateau, i.e., 35 K gauss in a 2.4-cm dia. bore at room temperature, uniform to 1 part in 1000 over a

distance of 1.5 cm, with a driving current of about 17A. A special power supply was used to drive this magnet, with features such as automatic sweep at a very low rate, and with various trigger devices to protect both the magnet and the power supply from dangerous voltage transients in case of accidental quenching of the superconducting coil.

4.2 Measurement of Electronic Gain

We now come to the important measurement of the small-signal electronic gain. This is the quantity that serves to validate the small-signal theory and, hence, our understanding of the device operation. All these measurements apply to a rectangular TE(101) resonator made from standard WR90 waveguide (No. 2 in Table 2.3). The coupling was magnetic, with a round iris placed in the narrow wall of the waveguide cavity. The resonator was driven with a 12-kV beam from a 1-mm dia. cathode, for the gain measurements, and with a 15-kV beam from a 2-mm dia. cathode, for the start-oscillation-current measurements.

To a reasonable approximation, a resonant cavity can be represented by the equivalent circuit of Figure 4.2, where $G_{sh}$ represents the wall losses and $G_{ext}$ the external loading (Ref. 26). The interaction of the beam with the cavity fields will cause a beam-loading conductance $G_e$ to appear in parallel with $G_{sh}$ and $G_{ext}$. At resonance, the reactive elements cancel and the VSWR looking into the cavity will be given by:

$$\text{VSWR (beam ON)} = \frac{G_{ext}}{G_{sh} + G_e} \tag{4.1}$$

When the beam is turned OFF, $G_e = 0$, and we have:

$$\text{VSWR (beam OFF)} = \frac{G_{ext}}{G_{sh}} \tag{4.2}$$

In Eqs. (4.1) and (4.2) we have implicitly assumed overcoupling, that is, $G_{ext} > G_{sh} + G_e$. For example, the X-band TE(101) cavity was overcoupled, and VSWR (OFF) = 4.7 in that case. If the cavity were undercoupled instead, then the reciprocals of Eqs. (4.1) and (4.2) would hold, so that VSWR > 1 always. Only the range $G_e < 0$ is of interest, and clearly VSWR (ON) will become negative when $|G_e| > G_{sh}$. Negative-resistance amplifiers have been discussed in the literature (Ref. 27).

Combining Eqs. (4.1) and (4.2), the beam-loading conductance becomes:

$$\frac{G_e}{G_{sh}} = \left( \frac{\text{VSWR (OFF)}}{\text{VSWR (ON)}} - 1 \right) \tag{4.3}$$

Oscillations will start when the beam-loading conductance becomes sufficiently negative to overcome both the cavity wall losses and the losses due to power coupled out of the cavity. However, a measurement of start-oscillation current does not give as complete a picture of small-signal behavior as a direct measurement of $G_e$, or electronic gain, under stable (non-oscillatory) conditions.

4-5

4.2.1 <u>Small-Signal Range</u>.- In order to determine just what level of the probing signal constituted a "small-signal" input to the device, the r.f. power emitted by the beam was measured as a function of drive level. This was done by comparing the power reflected from the cavity with the beam ON, to the incident power, i.e., the power reflected from a waveguide short.

The results show (Figures 4.3 and 4.4) that the gain mechanism saturates very rapidly, at drive power levels near 0.2 mW and with the output power at a level below 1% of the d.c. beam power. This result is very important, for it indicates a behavior typical for a maser amplifier, (Ref. 28). Interestingly, it was in terms of quantum electronics (Ref. 19) that the relativistic gain mechanism was first discovered, and spiraling-beam amplifiers were first referred to as cyclotron-resonance masers. This term later was avoided after the analysis of Hirshfield et al., (Ref. 9) had proven that a classical treatment was both possible and reasonable, at least for the linear region.

The buildup mechanism toward saturation can be explained heuristically in terms of Figure 4.2. If an r.f. voltage V is assumed to exist across the equivalent circuit, then the power emitted by the beam is given by:

$$P(\text{beam}) = (1/2) \ V^2 G_e \qquad\qquad (4.4)$$

But as we shall see below, $G_e$ is itself proportional to $V^2$, in the small-signal approximation, so that as the r.f. power level
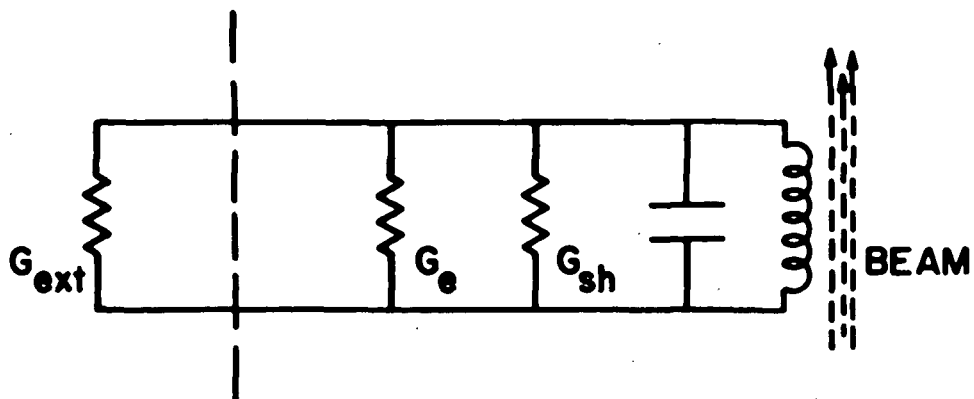
Figure 4.2.- Simplified equivalent circuit of a microwave resonator loaded both externally ($G_{ext}$) and by the presence of an electron beam ($G_e$).
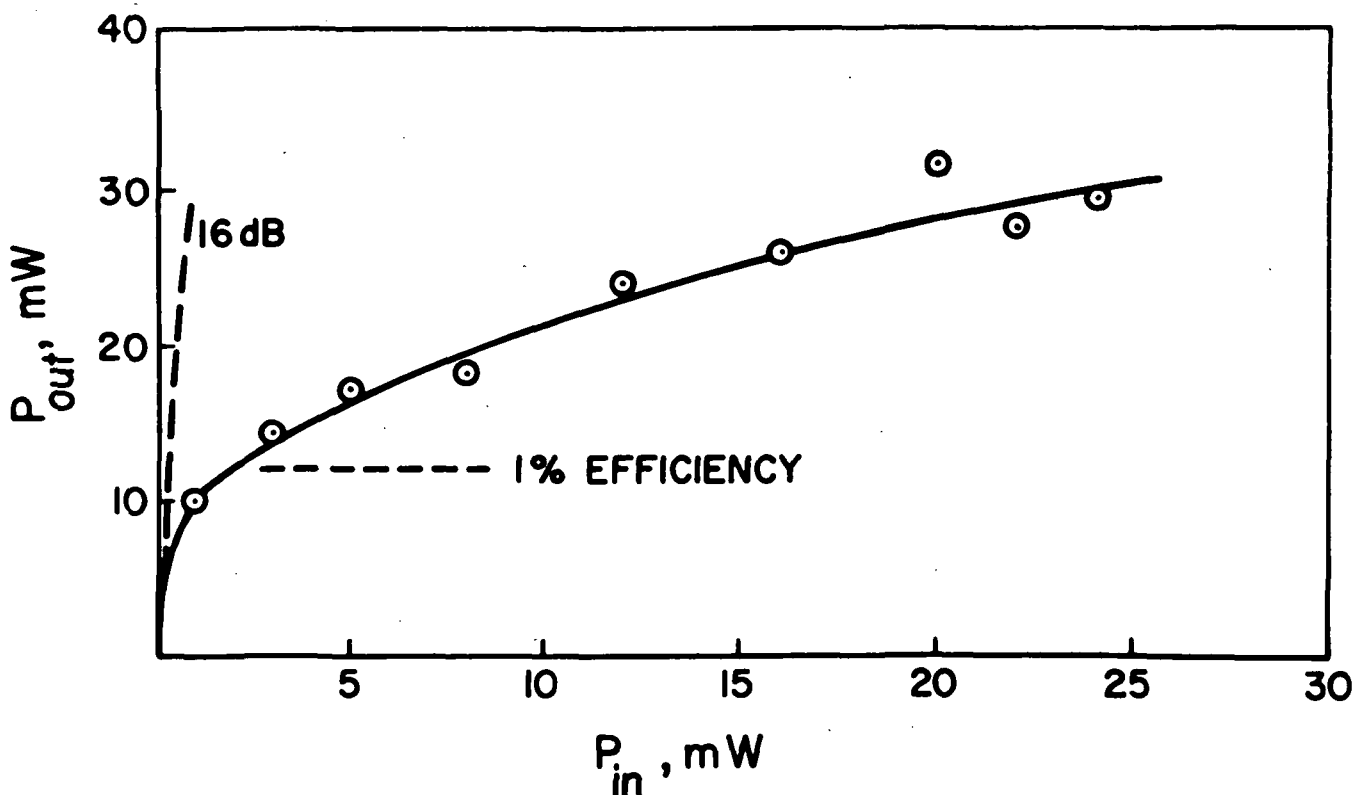


Figure 4.3.- Gain saturation characteristic, for the $TE_{101}$ resonator at $f_O = 9.460$ GHz, with $Q_L = 650$. Beam parameters are $V_O = 12$kV, $I_{coll} = 0.1$ mA, $I_{coll}$(max.) = 0.4 mA. The net r.f. power added by the beam, $P_{out}$, saturates at less than 3% of the d.c. beam power.
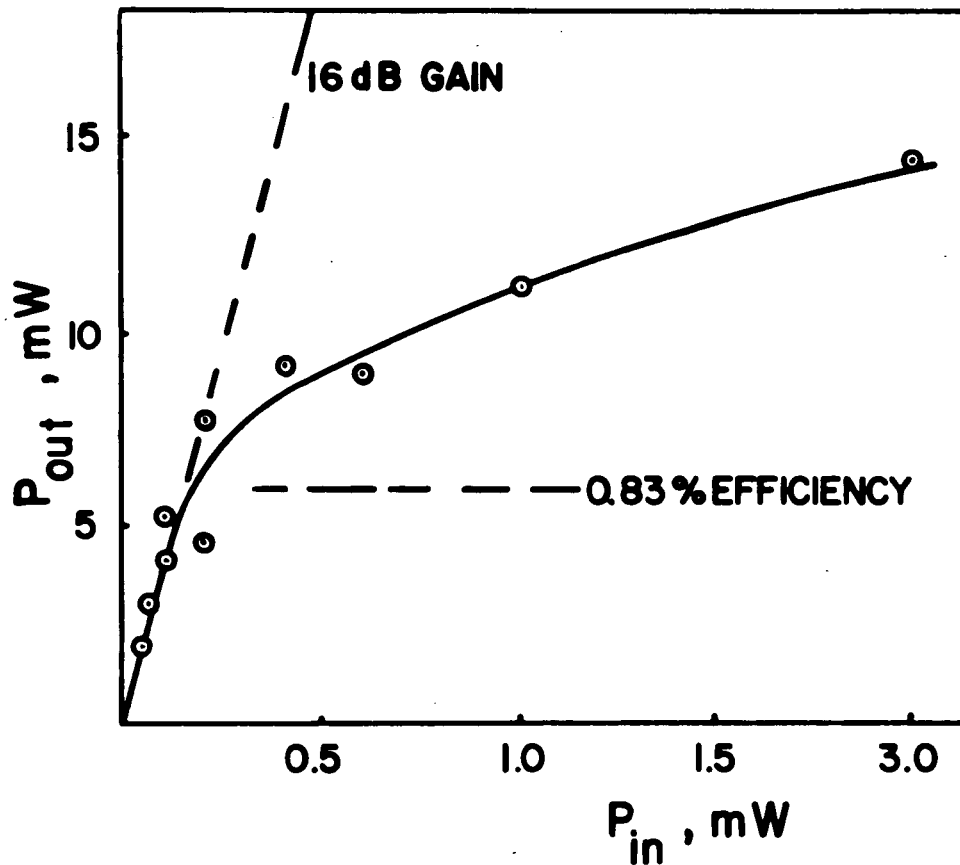
Figure 4.4.- Gain saturation characteristic, expanded version
of Figure 4.3. The collector current here is
$I_{coll}$ = 0.06 mA. Saturation begins at a drive
power level near 0.2 mW.

in the cavity increases, $G_e$ increases, which again raises the power level and $V^2$. Clearly this built-in feedback mechanism will continue until limited by nonlinearities.

The use of quantum-mechanics is a powerful tool in understanding the nature of these nonlinearities. The transverse-energy distribution of the spiraling d.c. beam represents a population inversion over a part of the ladder of closely-spaced Landau levels, corresponding to electrons orbiting in a confining magnetic field (Ref. 29). Each electron tends to relax to the next lower, less populated level, and in so doing emits a photon at the cyclotron frequency. In analogy with three-level maser action, one may designate the beam power flow $V_\perp \cdot I_{coll}$ represented by the transverse electron energies, as pump power. This quantity is kept constant in Figures 4.3 and 4.4. As the signal power increases, more and more downward transitions are stimulated, until eventually the populations are in equilibrium, and no more maser action is possible. If the input power is increased beyond this point, net power absorption may result, as some electrons are "pumped" back up to higher levels. This effect actually was observed experimentally with input power levels of less than a watt.

The fact that the gain saturates at an efficiency of less than 3% probably is not a basic device limitation, but rather is specific to this particular device and the relatively large energy spread of its beam. In effect, only a fraction of the

beam supplies non-equilibrium electrons, because the others are out of synchronism with the stimulating signal and hence do not participate in the maser action.

4.2.2 <u>Operation at a Multiple of the Cyclotron Frequency</u>. The simple model of Figure 4.2, with $G_e$ a negative, voltage-dependent conductance, makes it tempting to look for harmonic content in the output signal. The practical advantage of operating, for example, with only half the magnetic field, at a given frequency is obvious. A strenuous search was undertaken, in fact, to detect some interaction with the second harmonic of the cyclotron frequency, but this was unsuccessful. In terms of the maser model, second-harmonic interaction corresponds to quantum jumps between nonadjacent Landau levels (quadrupole transitions). The calculated probability of the latter, compared to the probability of the fundamental (dipole) transitions, turns out to be very small, and so one would not expect any harmonic output. It is possible, however, to design the resonator field configuration in such a way that the fundamental, purely circular cyclotron rotation of the electrons excites a higher cavity mode, and hence, a higher frequency of oscillation. Such an overmoded resonator was used successfully by Gaponov, et al. (Ref. 11), who excited the $TE_{0, 2, 1}$ mode in a circular-cylindrical cavity with a hollow-beam arrangement of individually spiraling electrons (see also Table 1.1). This approach probably could be extended to generate 4th or 5th harmonics of the cyclotron frequency, the

main limiting factor being the decreased interaction impedance as the mode order is increased.

4.2.3  Measurement of the Beam-Loading Conductance.- We now return to the actual measurement of $G_e/G_{sh}$. For comparison with the theory, it is necessary to convert the normalized-gain characteristics of Section 2 to curves of beam-loading conductance. Again referring to Figure 4.2, the r.f. power dissipated in the cavity walls is given by:

$$W_L = 1/2 \ V^2 G_{sh} \tag{4.5}$$

From this and Eq. (4.4), we find:

$$\frac{G_e}{G_{sh}} = \frac{P(beam)}{W_L} \tag{4.6}$$

where P(beam) has been given in Eq. (2.3).

The impedance term and the gain function have already been discussed, and there only remains $\rho(k_\perp a)$. For a TE$_{(101)}$ rectangular cavity, where the beam fills a very small part of the cross sectional area, we can write, approximately,

$$\rho(k_\perp a) \simeq \int_{beam\ area} (NdA) = \pi a^2 N \tag{4.7}$$

where N is the electron number density:

$$N = \frac{I}{\pi a^2 eu} \tag{4.8}$$

Furthermore, for a rectangular axial velocity distribution,
u here becomes $\langle u \rangle$, the arithmetic mean of the limits, so that:

$$\rho(k_\perp a) = \frac{I}{e\langle u \rangle} \qquad (4.9)$$

Using Eq. (2.15) to eliminate $W_L$, and substituting into
Eq. (2.3), there results, finally:

$$\frac{G_e}{G_{sh}} \cong \frac{\pi}{4} \cdot \frac{e}{mc} \cdot K \cdot \frac{I}{\langle u \rangle} \cdot (\text{N.G.F.}) \qquad (4.10)$$

which is the desired relation.

In measuring the beam-loading conductance, it was convenient
to sweep the magnetic field, and thereby to generate a curve of
$G_e/G_{sh}$ vs the slip parameter $\frac{\Omega - \omega}{\omega}$, or its negative. A set of
such measurements is plotted in Figure 4.5, together with theo-
retical curves that were derived from the normalized-gain charac-
teristics discussed in Section 2.

The relevant device parameters are listed below:

Frequency          = 9.460 GHz

Initial beam dia.  = 1 mm

Low-field strength  = 350 Gauss

High-field strength = 3433 Gauss  (center value)

Beam voltage       = 12 kV

Collector current (with $I_{cork}$ = 0)      $I_{coll}$ = 3.8 mA

                       (with $I_{cork}$ = 5.5A)  $I_{coll}$ = 2.3 mA

                       (with $I_{cork}$ = 6.25A) $I_{coll}$ = 0.53 mA
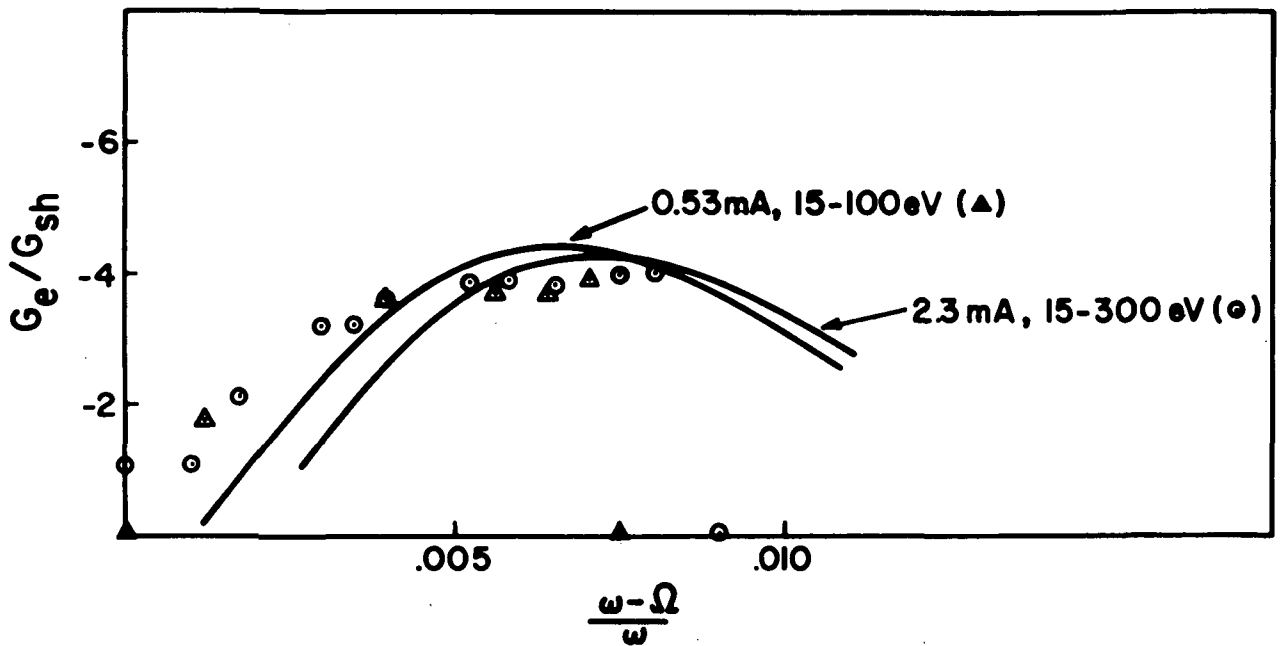
Figure 4.5.- Measured values of beam-loading conductance plotted over a range of the slip parameter. The data represent two different operating conditions with corkscrew current as the controlling parameter. The solid lines represent two of many possible fits of the theory to the data, with the assumed axial energy distribution as indicated. The abrupt drop in measured gain near $\Omega-\omega/\omega = 0.008$ is not understood. The probing-signal level was about 3 mW.

Cavity geometry   =   TE(101) rectangular, $\frac{\lambda}{\lambda_C} = 0.693$

Cavity impedance     K = 1.14 x $10^6$ ohms

Cavity $Q_O$ = 3600 (measured), $Q_L$ = 650

Estimated total velocity spread, before mirroring, $\frac{\Delta V}{V_O} \simeq 0.50$

As it was inconvenient during this measurement to use r.f. drive levels that were small enough to stay in the linear-gain region of the device, probing signal power levels near 3 mW were used. The resulting beam-loading conductance actually turns out to differ but little from the value corresponding to the observed small-signal gain of 16 dB (see Figure 4.3), which is $G_e/G_{sh} = -4.4$, and we, therefore, can reasonably use the slightly saturated (but easily measurable) values in Figure 4.5 as a basis for further discussion. The data shown in Figure 4.5 actually represent two different operating points, corresponding to corkscrew currents of 5.5A and 6.25A, respectively. As the corkscrew current is increased, a greater fraction of the beam is mirrored, and so the collector current decreases from a maximum of 3.8mA, for zero corkscrew current, to 0.53mA, for $I_{cork} = 6.25A$. This type of operation appears to be typical of beams generated by a corkscrew-mirror combination, and it is obviously wasteful of beam current. It does, however, reduce the effective velocity spread for that portion of the electrons which are not yet mirrored. The larger collector current corresponds to the inclusion of a greater portion of the energy distribution, and hence produces less average gain per electron than the smaller current.

The *measured* gain for both currents is about the same, however. As is seen in Figure 4.5, a reasonably good fit to these data can be obtained with theoretical gain curves based on an assumed axial energy spread of 0-100 eV for the smaller beam current and 0-300 eV for the larger current, with the active range for r.f. interaction extending from 15eV on upwards.

From the gain behavior illustrated previously in Figures 2.5 and 2.6, it is clear that any decrease in the calculated gain due to greater velocity spread, can easily be compensated by moving the lower limit of the "active" velocity range closer to the origin. The experimental data, therefore, could also be fitted with characteristics calculated for a wider energy range, which might actually be somewhat more realistic. For example, if the *total* estimated energy spread were 50%, then the observed mirroring action would result in estimated effective spreads of 840V and 3600V, respectively, assuming the model of Figure 3.4 to be correct. As both the effective spread and the lower limit of the active range are subject to conjecture, however, calculations were not pursued further. It has been demonstrated that the theory can be fitted to the experimental data, but without an accurate knowledge of the effective energy distribution an analytical prediction of the measured results is not possible.

The necessity of having to assume *a priori* an energy distribution could be eliminated if a measurement of the latter were possible simultaneously with the gain measurement. Such

measurements were attempted, using the magnetic mirror system itself to act as an energy analyzer, but they turned out to subject to large errors in the region of greatest interest, i.e., near zero collector current, because of current instabilities, and they were later abandoned. A commercially useful device would, of course, be designed to utilize the entire beam, with a specified, narrow velocity distribution. For such a device, the theory presented here probably can predict the small-signal gain with reasonable accuracy, subject only to a correct estimate of the lower limit of the energy range actually contributing to the gain. This estimate is not likely to vary from tube to tube, however, and presumably could be derived both from analysis and empirically.

It should be noted in passing that a rather high degree of uncertainty with regard to the axial drift motion of the spiraling electrons, appears to have characterized spiraling-beam amplifier work from the very beginning. Chow and Pantell (Refs. 2,5) allow for a 50% possible error in their estimate of the axial velocity, which was derived from a time-of-flight measurement, and their start-oscillation results naturally are subject to the same error. Hsu (Ref. 7) predicted Beasley's (Ref. 10) start-oscillation currents only to the correct order of magnitude, and incidentally, he was the first to point out the uncertainty that is introduced by an unspecified axial velocity distribution. Schriever, et al. (Ref. 6), also obtained order-of-magnitude estimates of the axial velocity, both from Doppler-shift and time-of-flight measurements,

but they made no attempt to get a detailed correlation with measured start-oscillation currents. The work reported here, therefore, constitutes the most accurate validation to date of the small-signal behavior of spiraling-beam amplifiers.

In order to test the effect of the probing-signal level on the measured beam-loading conductance directly, data were taken with the probing power reduced by a factor of 10, to $P_{in} = 0.3$ mW, and the results are plotted in Figure 4.6. Clearly, $G_e/G_{sh}$ reaches essentially the same maximum as before (Figure 4.5) but the magnetic line width has been reduced sharply.

4.2.4 <u>Start-Oscillation Current</u>.- The dependence of the small-signal gain on the beam voltage is illustrated in Figure 4.7 where the measured start-oscillation current is plotted as a function of $V_o$. This measurement refers to the same device used to generate Figure 4.3. For each beam voltage, the operating parameters were first adjusted to produce r.f. oscillations. The cathode was then temperature-limited to reduce the beam current, while both the corkscrew current and the high-field vernier control were adjusted continuously to maintain the oscillations down to as low a beam current as possible. The value of collector current where oscillations finally vanish is termed the start-oscillation current. Apparently, the optimum corkscrew-current adjustment to obtained simulates a velocity spread $\Delta V$ that is proportional to $V_o$, for the starting current in Figure 4.7 remains substantially constant with $V_o$, and this is precisely the behavior predicted for the small-signal gain from the analysis of Section 2.
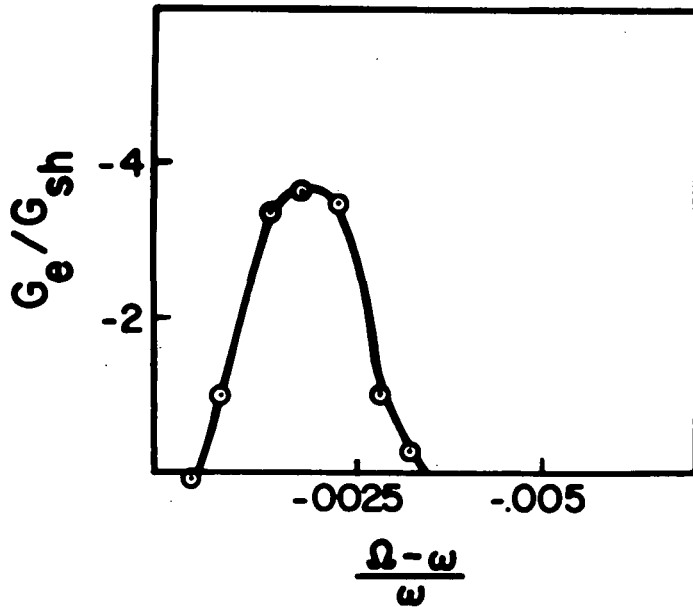
Figure 4.6.- Measured beam-loading conductance vs the slip
parameter.  The device is the same as in Figure 4.5,
but the beam current is $I_{coll}$ = 0.05 mA, and the
probing-signal level is 0.3 mW.  Note the much
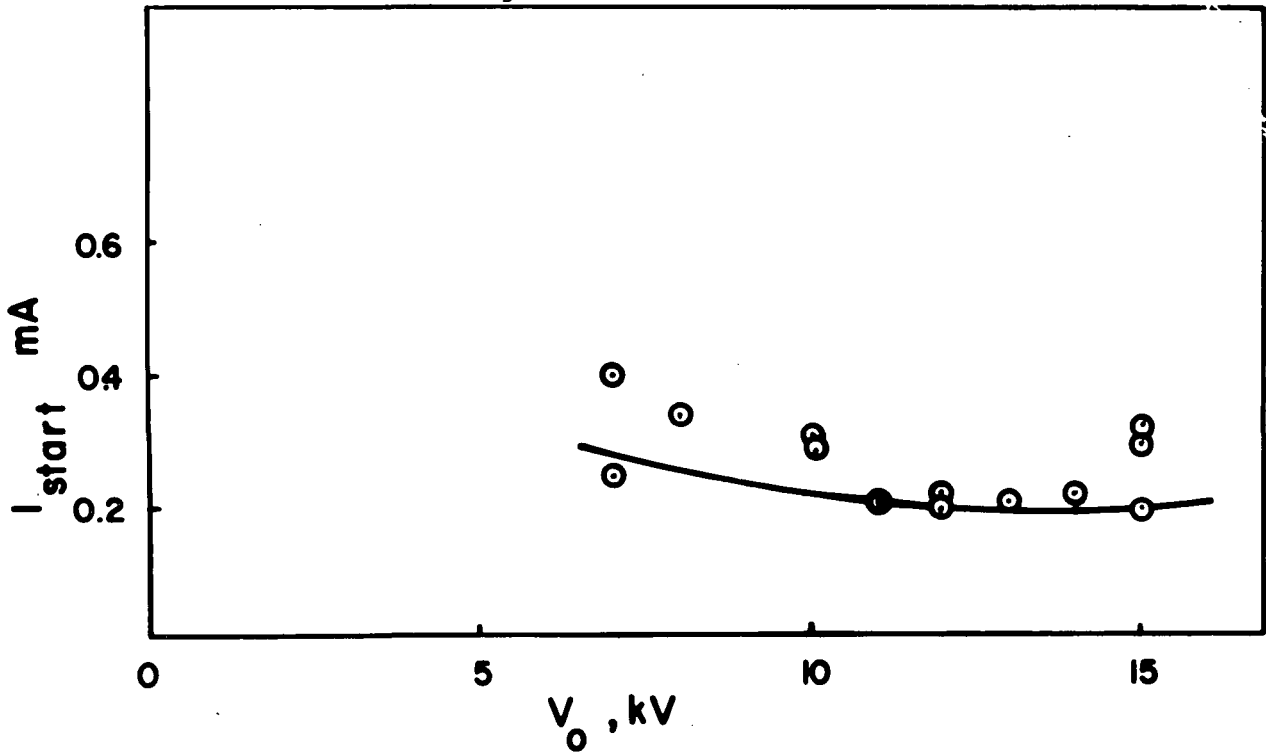narrower magnetic line width.



Figure 4.7.- Start-oscillation current vs beam voltage $V_O$, with
corkscrew current optimized for each $V_O$.  Data refers
to device of Figure 4.3.  No oscillations were
detected below a beam voltage of 7 kV.

(It should be noted that in order to operate with a given cork-screw at a beam voltage other than the design voltage, the axial magnetic field in the corkscrew region must be changed so as to satisfy Eq. (3.1) at all times.)  Figure 4.7 also confirms the existence of a gain threshold, such as was predicted in Section 2, near $V_o$ = 6 kV, as no oscillations could be observed at or below this voltage.

In previous work by the author (Ref. 17), the dependence of $I_{start}$ on the cavity loading has been investigated.  The results are reproduced in Figure 4.8. as a plot of $I_{start}$ vs the reciprocal of $Q_L$, where:

$$\frac{1}{Q_L} = \frac{1}{Q_o} + \frac{1}{Q_{ext}} \qquad (4.11)$$

In terms of the simple model of Figure 4.2, the start-oscillation condition corresponds to $|G_e| \geq G_{sh} + G_{ext}$, where $|G_e|$ is proportional to the beam current.
But clearly, from their definition:

$$G_{sh} + G_{ext} \sim \frac{1}{Q_L} \qquad (4.12)$$

and, thus, one finds:

$$G_e \sim \frac{1}{Q_L} \sim I(beam) = I_{start} \qquad (4.13)$$

and this linear relationship between the start-oscillation current and $1/Q_L$ is confirmed by the data of Figure 4.8.  However, the linearity demonstrated in Figure 4.8.applies only to the
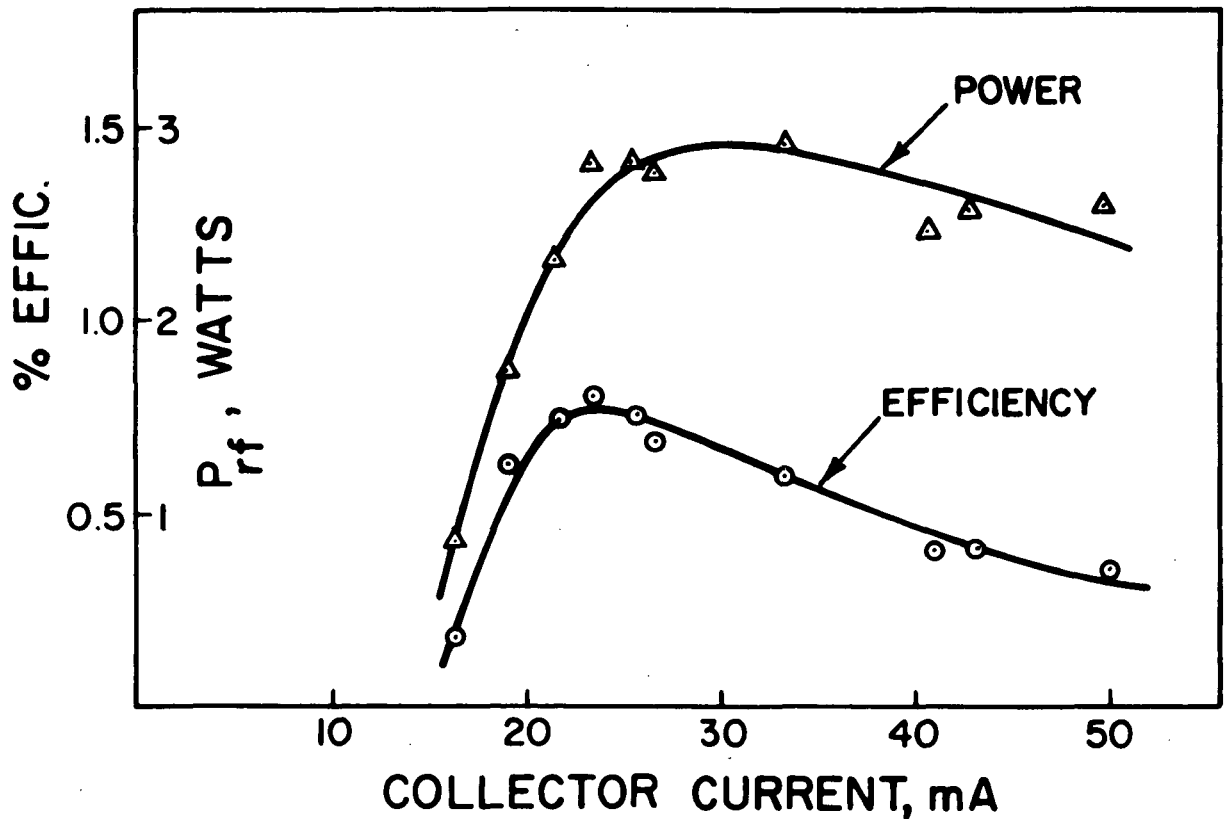
Figure 4.8.- R.F. output power and efficiency for a TE$_{101}$ resonator at 9.46 GHz, with $\lambda/\lambda_c = 0.693$. The beam voltage is 15 kV and the cathode diameter is 2 mm. Corkscrew tuning and current were adjusted to produce maximum output power at each point, while the collector current was controlled by temperature-limiting the cathode.
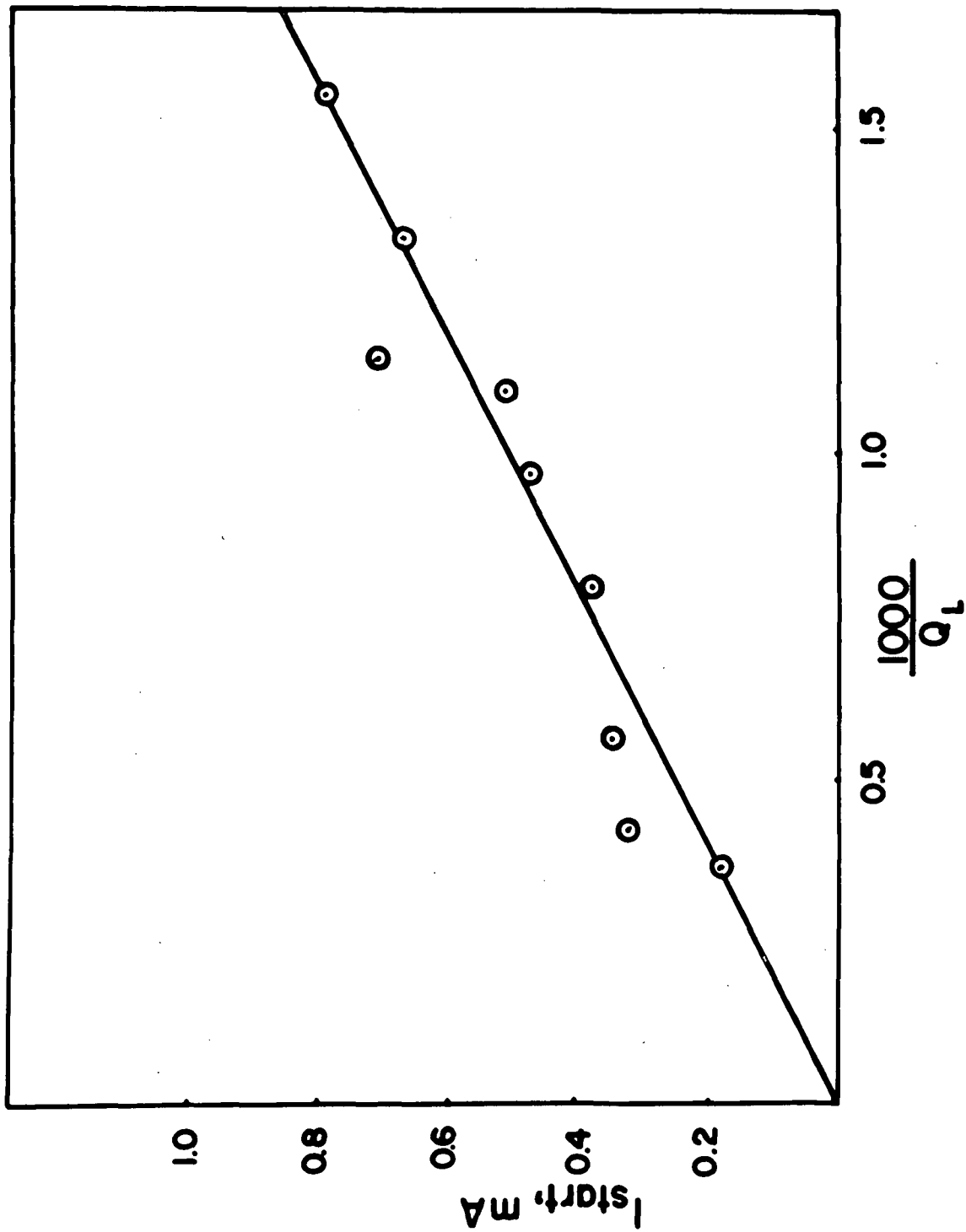
Figure 4.9.- Start-oscillation current vs $1/Q_L$, for a TE(101) resonator at 9.43 GHz. The beam voltage is $V_O$ = 15 kV. (After Ref. 17).

superposition of the individual electron emissions, i.e., it confirms the absence of r.f. space-charge effects. It does not contradict the observed saturation behavior of the r.f. gain mechanism, i.e., the phase focusing of the electrons, which has been shown to be a phenomenon quickly limited by a nonlinearity, i.e., the saturation of Landau levels.

In summary, the measurements indicate that the electronic gain of spiraling-beam amplifiers saturates quickly. Nonetheless, the measured magnitude and the magnetic linewidth of the negative beam-loading conductance can be fitted well by calculations based on the linearized small-signal model, provided that an appropriate axial energy distribution is assumed. A direct measurement of the latter is very difficult in the region of greatest interest, i.e., at near-zero axial velocities. The linearized theory, therefore, can be used to optimize the device design parameters, but it cannot in general predict exact device performance. Measurements of the start-oscillation current confirmed the absence of r.f. space-charge effects and also the near-independence of the electronic gain on the beam voltage in the presence of velocity spread. Harmonic components in the output signal are negligibly small compared to the fundamental.

4.3 Power and Efficiency

Under large-signal conditions, the interaction between a spiraling electron beam and a microwave field can no longer be described by the linearized theory. Attempts have been made to

predict the large-signal behavior by including some nonlinear terms in the small-signal equations (Ref. 7) or by direct integration of the relativistic equation of motion (Ref. 18). In either case, the expressions quickly become cumbersome mathematically, and difficult to keep track of physically. We shall therefore present only measured results, and then attempt to generalize these results by drawing on the physical insight gained earlier from the small-signal model.

From Figures 4.3 and 4.4., it already has become evident that the gain mechanism saturates quickly, at output power levels of the order of 1% of the d.c. beam power. It is evident, therefore, that this gain mechanism does not respond well to strong driving fields. This is unlike the axial-bunching mechanism used in linear beams, where the best efficiency has been achieved with klystrons (intense electric-field modulation of the beam over short distances) as opposed to traveling-wave tubes (moderate-intensity interaction over extended distances.) Here one is led to the conclusion that spiraling-beam interaction takes place more efficiently over long distances, with relatively moderate driving field amplitudes. This conclusion is confirmed by the successful traveling-wave design that was reported by Schriever and Johnson (Ref. 3), which yielded an efficiency of eight percent.

Measurements of oscillator efficiency were made with a number of different beams, all operating with a TE(101) resonator (No. 2 in Table 2.3) at 9.46 GHz, at $\lambda/\lambda_c = 0.693$. All the beams

were generated in the basic arrangement of Figure 3.1, but with different cathode diameters. The r.f. power output was measured by using a carefully calibrated 10- or 20-dB directional coupler in series with a precision calibrated attenuator and a calibrated crystal. Dependence on the crystal law was eliminated by always driving the crystal to the same operating point, as observed by the pulse height displayed on the oscilloscope, and using only the precision attenuator to determine relative power levels. The efficiency was defined in terms of the r.f. power and the product of beam voltage and collector current, ignoring that part of the beam which was mirrored before reaching the cavity. Figure 4.9 plots the r.f. power and the efficiency as a function of the collector current, for a 15-kV beam with a 2-mm cathode diameter (Ref. 17).

The current variation shown in Figure 4.9 was achieved by changing the voltage on the control anode and by adjusting the heater voltage, while the corkscrew and low-field currents were adjusted to give maximum power output at each point. The saturation and roll-off of both curves, therefore, reflects the saturation of the gain mechanism as well as the effects of changing velocity spread.

The peak efficiency shown in Figure 4.9 is less than one percent. This was improved upon in later measurements by using a thinner beam (1-mm cathode diameter) which had a total energy spread estimated at 50%, probably less than the earlier,

thicker beam. These later results are plotted in Figures 4.10 and 4.11.

The r.f. power output is seen to rise monotonically to saturation, accompanied by an increasing scatter in data points. The efficiency drops monotonically from a peak value near one percent, as the collector current is increased. This peak efficiency is of the same order as that found earlier when the device was operated as an amplifier, at incipient saturation.

It should be noted that in the cases shown in Figures 4.10 and 4.11, the collector current was controlled by varying the corkscrew current, with the low-field plateau adjusted to a constant value greater than the corkscrew resonance, in order to produce the narrowest possible velocity distribution. In terms of the simple model of Figure 3.4, the effective velocity spread is thus proportional to the collector current, and the average gain per electron decreases as the current is increased.

A typical set of oscillograms of the more important operating variables is given in Figure 4.12. It may be noted that while the r.f. pulse amplitude reflects the droop in the supply voltage pulse, there are no amplitude instabilities of the type that were observed in an earlier device (Ref. 17). The earlier instabilities had been identified as being due to ion oscillations, and it is possible that these were related to ripples in the high-field plateau (see Figure 3.1), which were not present in the Helmholtz system used here. A further difficulty apparently
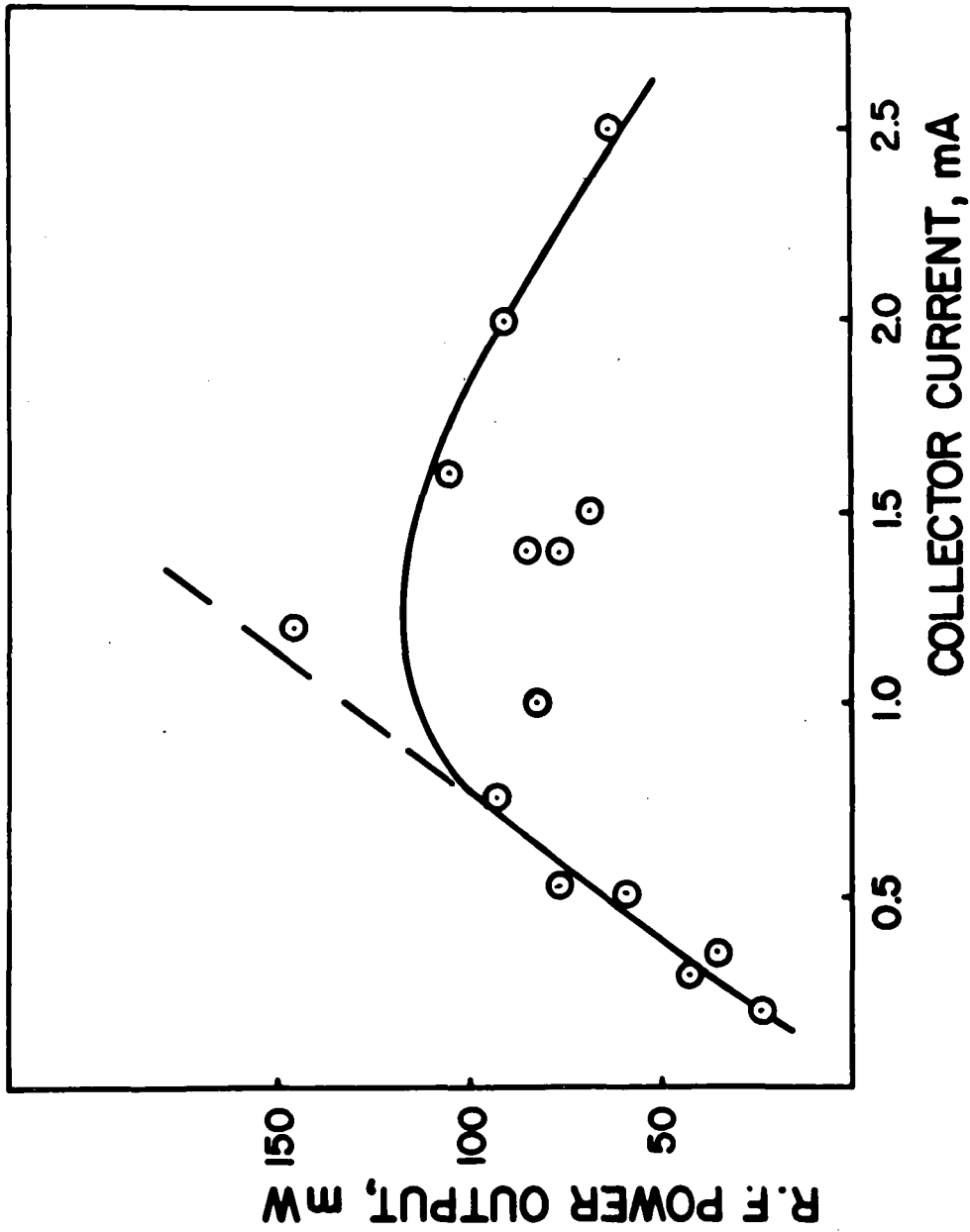
Figure 4.10.- R.F. power output for TE(101) oscillator at 9.46 GHz, with $\lambda/\lambda_c = 0.693$. The beam voltage is 12 kV and the cathode diameter is 1 mm. The collector current was controlled by varying the corkscrew current, with the low field set to a value 10% above the corkscrew resonance.
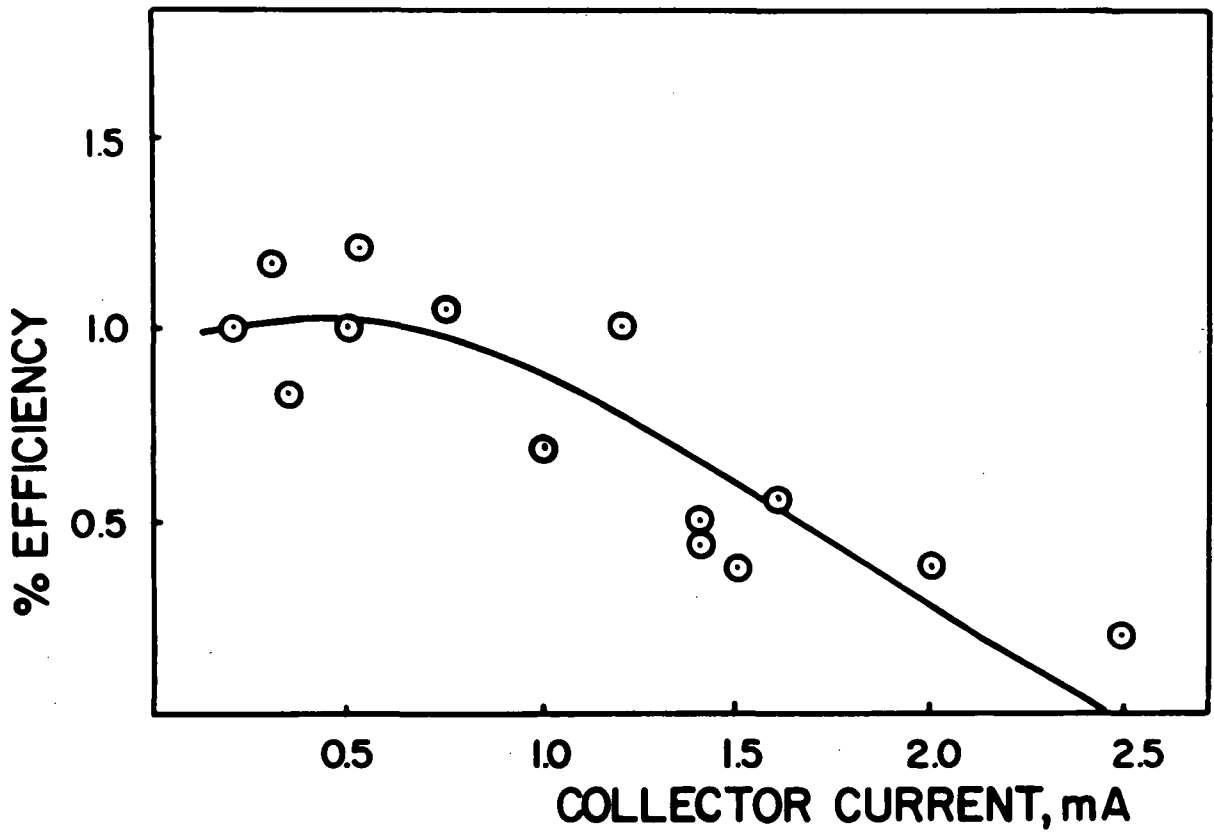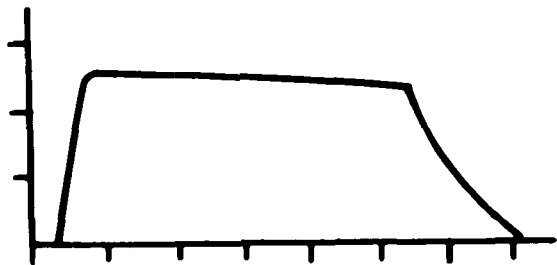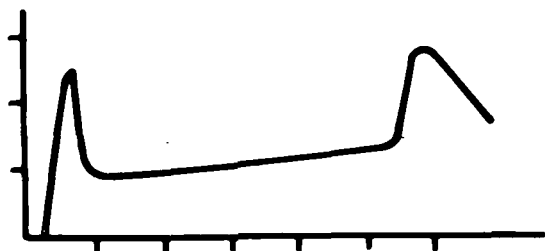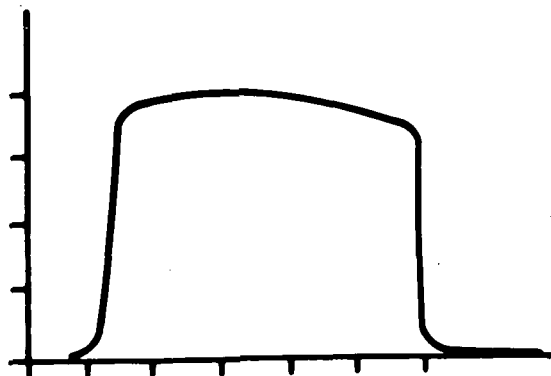
Figure 4.11.- Efficiency vs collector current, calculated from the data of Figure 4.10.

**D.C. VOLTAGE PULSE**
   **5 kV / DIV.**
   **(12 kV NOMINAL)**
**HORIZONTAL SCALE 5 $\mu$ SEC./DIV.**

**COLLECTOR CURRENT PULSE**
   **ImA / DIV.**
   **(1.2 mA NOMINAL)**

**ATTENUATED RF POWER PULSE**
   **(VOLTAGE SIGNAL FROM SQUARE-**
   **LAW CRYSTAL)**
   **5 mV / DIV.**

Figure 4.12.- Oscillograms of typical pulse shapes on the TE(101)
              resonator device, driven by a 12 kV beam launched
              from a 1 mm dia. cathode. The corkscrew current
              was 8.4 A, and the low field plateau was set at
              nearly 10% above the corkscrew resonance. The max.
              collector current is 4 mA, and this is reduced to
              1.2 mA by the magnetic mirroring action. The d.c.
              voltage pulse has some droop which is reflected both
              in the collector current and in the domed appearance
              of the r.f. output pulse.

4-28

avoided by changing to the Helmholtz system was the occurrence

of an r.f. breakdown phenomenon that occasionally had limited

or blocked oscillations in the early device.

A plot of oscillator efficienvy vs beam voltage is given

in Figure 4.13, showing an approximately linear increase with

$V_o$. This result contrasts with the data of Figure 4.7, which

indicated that the *small-signal* gain was essentially independent

of voltage. However, both results should be interpreted with

some caution, because the velocity distribution in Figure 4.13 was

optimized for each point, and hence, enters as an uncontrolled

variable.

With many electron devices, a certain amount of experimental

adjustment can produce amazing results, and the spiraling-beam

oscillator is no exception. In an attempt to raise the efficiency

of the early TE(101) device at X-band, much effort was spent to

eliminate the ripples in the high-field profile by judicious

juggling of solenoid spacings and currents. One of the resulting

field profiles in the resonator region is shown in Figure 4.14,

and this turned out to produce very good results which are

summarized below.

> Resonator: TE(101) rectangular = 9.466 GHz
> Pulse length = 12 $\mu$sec at 60 pps
> $V_o$ = 15 kV Cathode dia. = 2 mm
> $I_{coll}$ = 25 mA with corkscrew off
> $I_{coll}$ = 5 mA with $I_{cork}$ = 10.5 A
> R.F. output = 5.0 W
> Electronic efficiency = 6.7%

The high efficiency is misleading, unfortunately, because

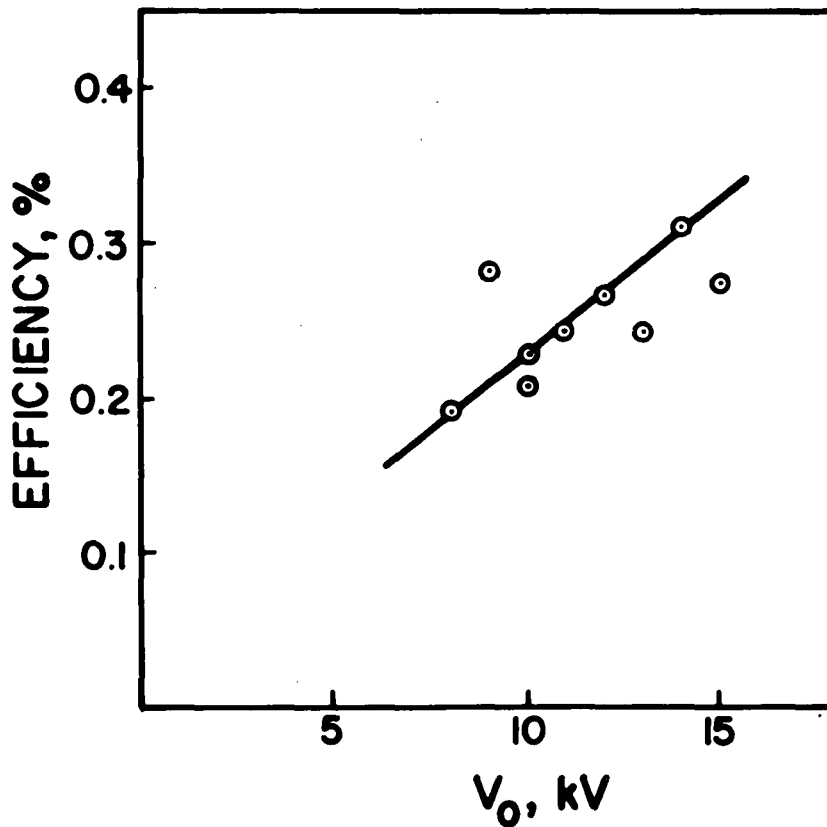from the field profile it is clear that some mirroring could take

Figure 4.13.- Oscillator Efficiency vs beam voltage, with the beam from a 3 mm dia. cathode, operated at constant perveance $6.5 \times 10^{-8}$ $AV^{-3/2}$, and a TE(101) resonator at 9.46 GHz. The low field amplitude was adjusted to track the corkscrew resonance, and the corkscrew current was optimized for max. r.f. output at each beam voltage. Collector current typically was 10% of the cathode current, with some interception at the control anode.
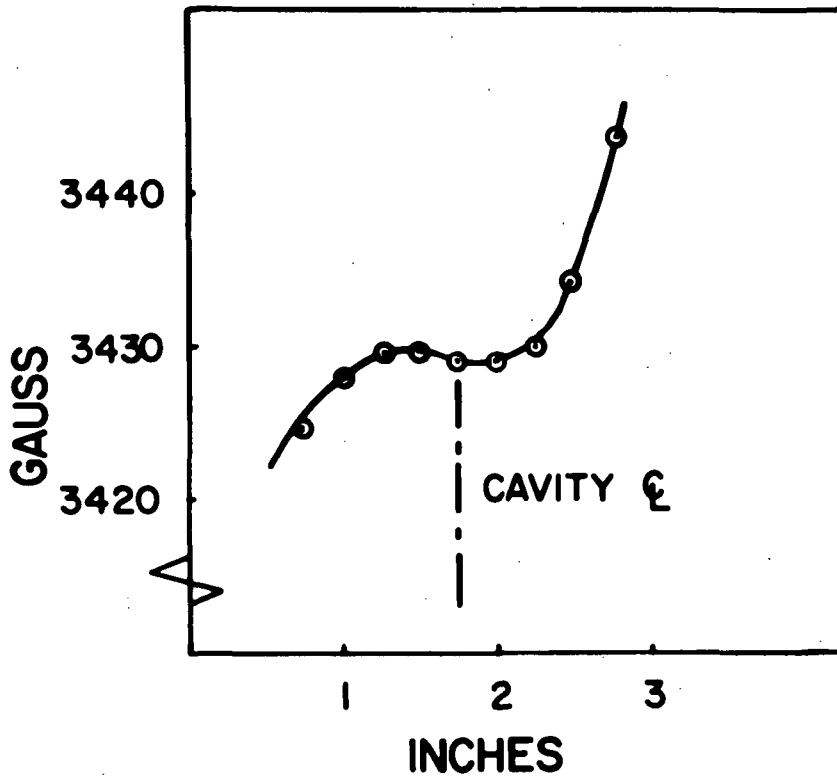
Figure 4.14.- Magnetic field profile near the TE(101) resonator
that produced the greatest observed power and
efficiency.

place between the cavity and the collector, spaced 3 cm behind

the cavity center line.  The collector current, therefore, is

likely to be less than the current actually driving the cavity,

and this may account for the large apparent efficiency.  The

output power level, however, is accurate, and it represents an

improvement over the earlier measurement plotted in Figure 4.8.

A further result in this category was obtained with the

same cavity, driven by a 12 kV beam from a 1-mm dia. cathode.

The other parameters were:

$I_{coll}$ = 18.5 mA with corkscrew off

$I_{coll}$ = 1.4 mA with $I_{cork}$ = 10.5 A

RF output = 363 mW

Electronic Efficiency = 2.16%

This result was obtained with the regular, flat high-field

plateau.  It should be realized also that the r.f. output power

levels quoted in this report represent actual measured power.

If, as is sometimes done, one were to include the power dissipated

in the resonator walls as part of the total r.f. power produced,

this would increase the quoted values of power level and efficiency

by about 20%.

In summary, the X-band measurements of oscillator efficiency

closely duplicated the earlier results for amplifier efficiency.

This further confirms the picture of the gain mechanism as being

maser-like, with the r.f. output saturating as the population

inversion of the available Landau levels is depleted.  However,

the density of inverted Landau levels in the correct axial energy range can be improved by better beam design, and the measured efficiencies near 1% are not an upper limit. Traveling-wave interaction appears to produce greater efficiencies than resonant interaction. Some evidence has been observed indicating an increase of efficiency with beam voltage.

## 4.4 A Cyclotron Resonator Tube at 94 GHz

Several devices were built and tested to demonstrate feasibility near the 94 GHz atmospheric window and to explore the performance limitations in this frequency range. The basic experimental arrangement closely resembles that of the earlier X-band setup, as shown in Figure 3.1. The strong magnetic field (35k Gauss) required to support cyclotron resonance here was generated with a superconducting solenoid that had a 2.4-cm dia. room-temperature-access bore. The low-field plateau was derived from a regular water-cooled solenoid, 76-cm long x 10-cm in. diameter.

The first device that produced measurable r.f. interaction utilized a single resonated section of WR-10 waveguide in the TE(1,0,12) mode, and this cavity was probed with an r.f. signal at and near the resonant frequency. The 5-kV beam was derived from a 3-mm dia. cathode. Due probably to poor alignment in the gun region, there was enough residual rotation on the beam to cause cyclotron-resonance absorption and emission effects in the cavity, even with the corkscrew modulation turned off. Applying

drive current to the corkscrew in fact weakened these effects, probably because the corkscrew modulation was out of phase with the inherent beam rotation.

A later experimental tube gave better results. This tube is sketched to (axial) scale in its magnetic field profile, in Figure 4.15, and some design parameters are listed in Table 4.1.

It may be noted that despite the much higher design frequency, the nominal interaction impedance of this cavity is only slightly smaller than that for the earlier X-band cavities, thanks to more careful design. The high-field plateau had an axial uniformity of one part in 1000 over a 1.5-cm distance, extending well beyond the 4.1-mm cavity length. The temporal stability of the high-field plateau was determined by the power supply regulation, 1 part in $10^5$, and was even better when the solenoid was operated in the persistent mode.

The beam in this tube was thinner than before, and hence, less sensitive to transverse inhomogeneties of the corkscrew field. The corkscrew itself was allowed to extend for some distance into the ramp region, so that the final portion would run slightly above cyclotron resonance. The result was a beam with a relatively narrow energy distribution, as measured by using the magnetic ramp as a velocity analyzer (Refs. 24, 25). That is, with a corkscrew current of 3A, the axial energy spread at the corkscrew exit was found to be only 2.2%. However, this spread was then multiplied by the magnetic mirror ratio, so that
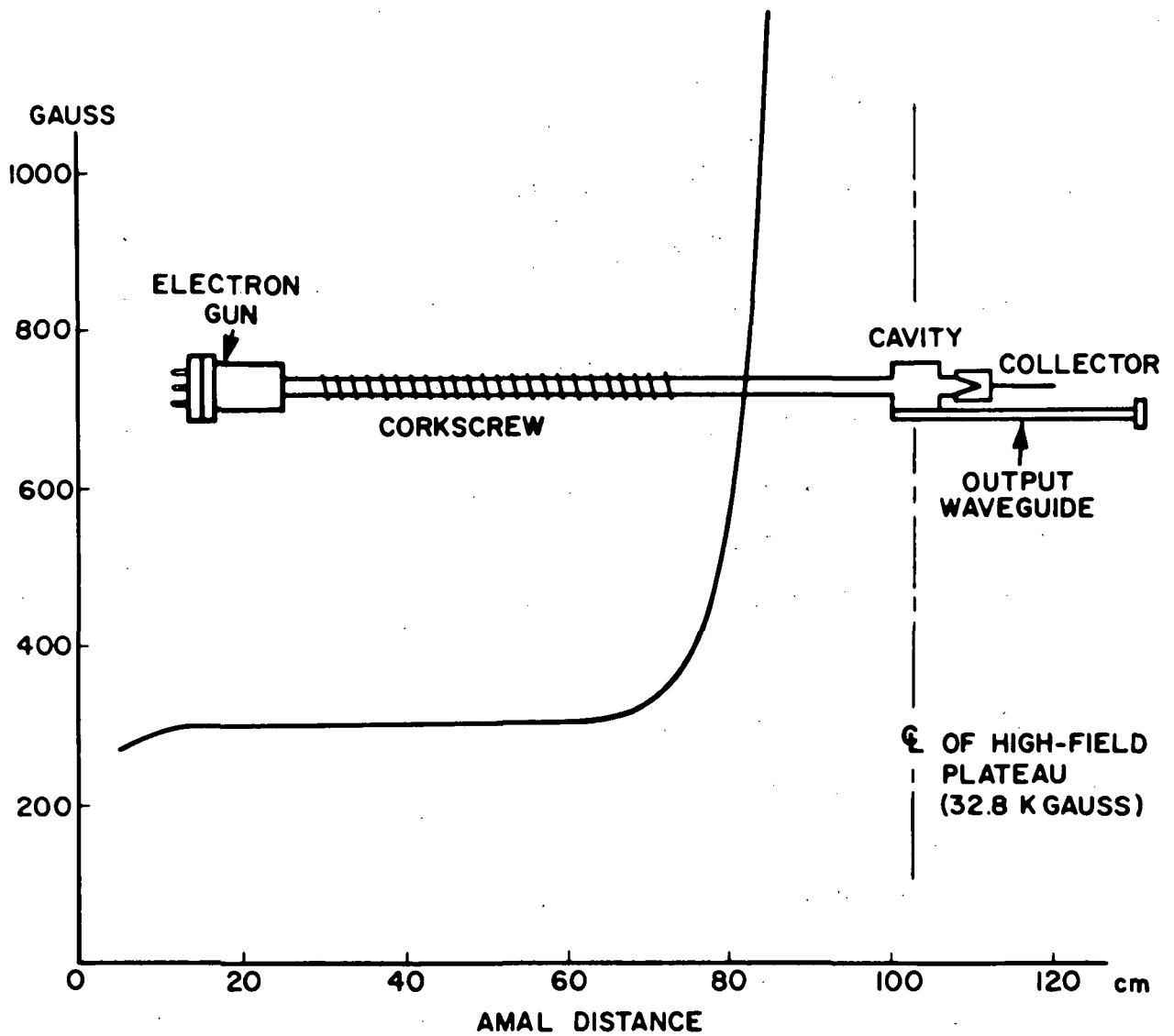
Figure 4.15.- A 94 GHz cyclotron-resonance tube with its
associated axial magnetic field profile. The
axial dimensions are drawn to scale. Only the
low-field plateau and a portion of the magnetic
ramp are shown.

4-35

## TABLE 4.1.- DESIGN PARAMETERS FOR A 94 GHz CYCLOTRON RESONANCE TUBE

Beam Voltage, 10 kV

Cathode current, 32 mA for 70 μsec at 60 pps

Cathode diameter, 1 mm, temperature - limited

Current density, 13 A/cm$^2$ (pulsed)

Collector current, 12 mA without corkscrew action

Collector current, 4 mA with corkscrew current, 8A

Corkscrew length, 43 cm (quadrufilar)

Corkscrew diameter, 1.59 cm

Corkscrew pitch, 3 cm

Low field intensity, 700 Gauss ± 10 Gauss

High-field intensity, 32,650 Gauss (nominal)

Cavity resonance, 92.59 GHz, TE(011 cyl.) mode

Cavity undercoupled with VSWR = 3.5

Theoretical $Q_O = 5000$

Loaded $Q_L \geq 1300$ (est.)

Cavity impedance, K = 0.32 x 10$^6$ ohms

Cavity dimensions 4.1 mm dia. x 5.3 mm long

Cavity position optimized for max. r.f. gain

in the interaction region it would have been 100-200 percent,
if the simple theory is assumed to hold. The beam passed through
the cavity through 0.8-mm dia. off-center axial openings at the
radial position of maximum transverse electric field strength,
and the presence of these openings decreased the resonance
frequency from a nominal 94 GHz to 92.59 GHz.

The cavity was probed with an external C.W. signal derived
from a reflex klystron that was tuned to the cavity resonance.
The presence of beam current in the cavity was signaled by a
level change in the r.f. power reflected from the cavity, which
would last for the duration of the beam pulse. As the cavity was
undercoupled to begin with, $G_{sh} > G_{ext}$, and the addition of a
negative beam-loading conductance (net r.f. power emission from
the beam) would bring the cavity closer to the critical-coupling
condition, $G_{sh} + G_e = G_{ext}$. Thus the reflected-power level
would *decrease*. Similarly, it would *increase* for the case of
net r.f. power absorption by the beam. Figure 4.16 shows some
typical pulse shapes. The largest change in reflected-power
level for the emissive phase was measured as 3.0 dB, and this
represents an electronic gain. The absorptive phase, which was
reached by a slight decrease in magnetic field, gave a comparable
result. The approximate equality of emission and absorption
peaks and the dependence of these peaks on magnetic tuning and
on the corkscrew excitation are all as expected from the analytical
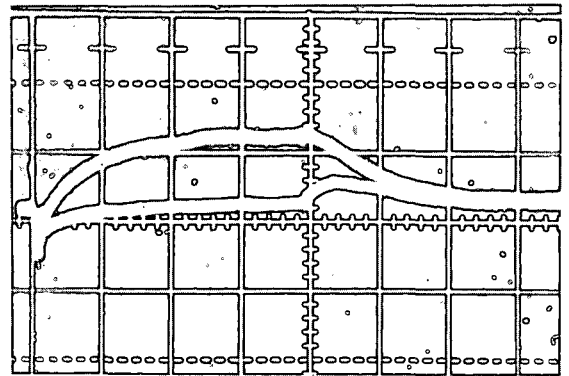results derived previously, and thus, they indicate that the tube
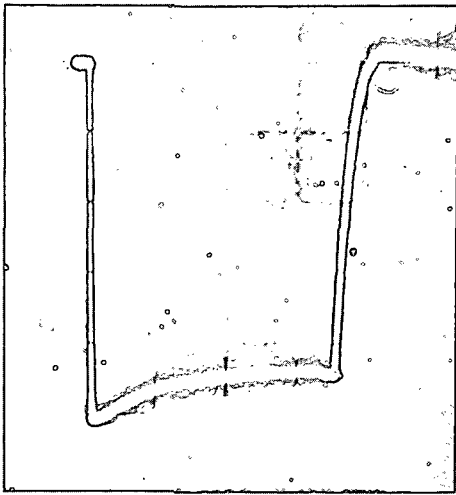
$V_0$ (2kV/div.)
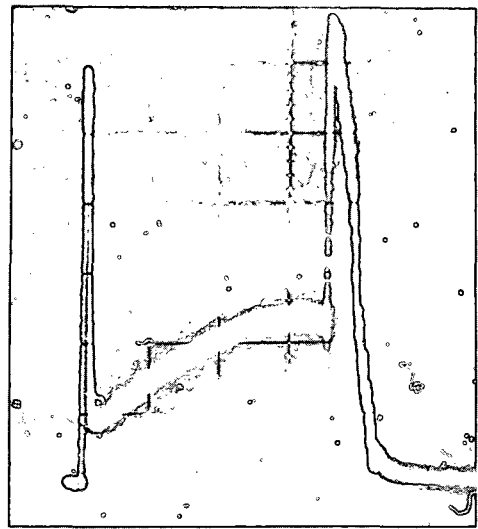


$I_{COLL}$(2mA/div.)
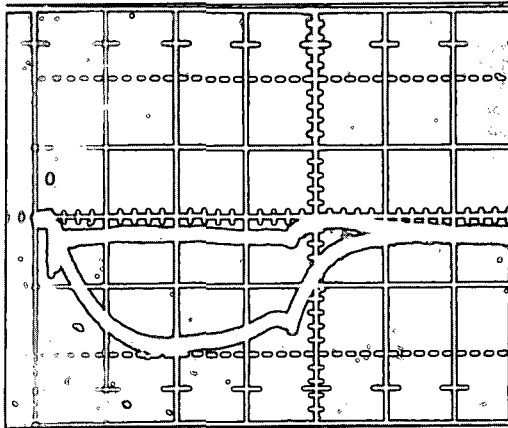


REFLECTED SIGNAL
(EMISSION)
$I_{CORK}$ = 0 and 8A



REFLECTED SIGNAL
(ABSORPTION)
$I_{CORK}$ = 0 and 8A

Figure 4.16.- Oscillograms of typical waveshapes that show
emission/absorption at 92.6 GHz. The time
scale is 20 μsec/div.

essentially was operating as intended.  The small observed gain
can be understood in terms of the large velocity spread on the
beam, and an approximate calculation confirms this, as follows.

If the energy spread due to the corkscrew is estimated at
3%, then with a mirror ratio of 50 the spread in the interaction
region would be 150%.  The average height of the collector
current pulse is 12 mA without corkscrew modulation and decreases
to 4 mA with $I_{cork}$ = 8A.  Clearly, the magnetic mirror action
cuts off any electrons that leave the corkscrew with more than
2% of their energy in the transverse direction, and two-thirds
of the total number of electrons are in that range.  The
remaining electrons, therefore, must occupy the transverse energy
range between 0.01 $V_O$ and 0.02 $V_O$ at the corkscrew exit, and
between 0.5 $V_O$ and $V_O$ in the interaction region, i.e., the
the effective energy spread is 50%, or $\Delta V$ = 5000 V.  Looking back
at Figure 2.8, it is seen that the normalized gain function
decreases as $1/\Delta V$.  It is not surprising, therefore, that with an
estimated $\Delta V$ = 5000 V, the gain is very small.  On the other
hand, the fact that the device behaved qualitatively as expected
leads one to believe that satisfactory gain and oscillation can
be obtained, once the problem of energy spread on the beam is
brought under control.

A few further remarks are in order concerning the experi-
mental techniques.  It was found that in order to lock the device
into either the emissive or the absorptive phase, the super-

conducting solenoid had to be swept at an extremely slow rate, and when the desired point was reached (3265 Gauss nominal), the magnet was quickly put into the persistent mode, for best stability. The strong sensitivity to magnetic tuning derives from the fact that the slip parameter $\frac{\Omega-\omega}{\omega}$ which enters as the independent variable in the absorption emission characteristic such as Figure 2.2, arises as the difference of two large numbers.

Two different mirror ratios were used, 47 and 110, corresponding to low-field intensities of 700 and 300 Gauss, and calling for corkscrew pitch lengths of 3 cm and 7 cm, respectively. The gain was substantially the same for either of these beams.

By raising the cathode temperature, it was possible to increase the collector current to 25 mA and above, with the 700 Gauss low-field plateau, but no increase in gain was observed. Also, beam transmission became poor and the collector pulse began to show strong instability, probably indicating the presence of ion oscillations. The vacuum generally was maintained at $10^{-6}$ $T_{orr}$, or better, by an attached 1ℓ ion getter pump. Apparently the great current densities in the gun and low-field region also produced a greater velocity spread, thereby canceling the intended effect of providing a greater density of energetic electrons with near-zero axial velocities.

# 5. CONCLUSIONS

This report has described an in-house exploratory development program concerned with millimeter and submillimeter wave generation and amplification with devices where a thin, solid beam of individually spiraling electrons of moderate energy (10-20 kV) interacts at the cyclotron frequency with the transverse electric field of a smooth waveguide or cavity. While the bulk of this effort has been devoted to the observation and analysis of the device performance at X-band, some experimental work also has been done to prove feasibility at 94 GHz.

Power outputs near 5W and electronic efficiencies near 3% were obtained at X-band and moderate gain was observed at 94 GHz. The small-signal theory gives a good fit to the X-band data, and the device behavior at 94 GHz also is explained by the theory. The performance is limited chiefly by the velocity spread in the spiraling electron beam, and once this problem can be brought under control, high-power generation of millimeter waves appears quite feasible with this type of device.

R. F. space-charge effects appear to be negligible, but d.c. space-charge forces apparently prevent axially slow-moving electrons from participating in the r.f. interaction, and for this reason a hollow-beam geometry is to be preferred. The quick saturation of the r.f. gain mechanism implies that extended-interaction regions (waveguides or long low-Q cavities) are likely to yield better efficiencies than the high-intensity fields of short-cavity resonators, and the results reported in the literature confirm this point.

A decrease of the efficiency at higher frequencies is to be expected, mainly because as the axial magnetic-field intensity is raised, the width of the energy spectrum of the spiraling electrons tends to increase also. However, operation at integral multiples of the cyclotron frequency has been reported with over-moded schemes, i.e., by designing the electromagnetic field configuration such that the fundamental cyclotron rotation couples to some waveguide or cavity mode at a harmonically related frequency. This approach in one case reportedly has yielded an electronic efficiency of 3%, by exciting the cylindrical TE(0,2,1) mode at 25 GHz, corresponding to the second harmonic.

The efficiency tends to increase as the beam voltage is raised. However, a major advantage of this type of device is precisely the fact that operation with moderate beam voltages (10-20 kV) is possible, so that elaborate high-voltage power supplies or r.f. pumping schemes are not required. The most fruitful approach to raise the efficiency would seem to be by controlling the width of the electronic energy spread, and by maximizing the interaction impedance of the r.f. structure.

In summary, the analytical and experimental results indicate that the spiraling-beam device represents a feasible approach towards generating watts of c.w. power at mm and sub-mm wavelengths, provided that ways can be found to generate beams that have a narrow energy spectrum. Any further development effort should address itself first and foremost to this problem.

REFERENCES

1. Kulke, B.:  Millimeter-Wave Generation with Electron-Beam Devices, NASA Technical Note TN D-3727, February 1967.  Also, Microwave J. vol. 10, Sept. 1967, pp. 45-53 (with C. M. Veronda).

2. Chow, K. K., and Pantell, R. H.:  The Cyclotron Resonance Backward-Wave Oscillator.  Proc. IRE, vol. 48, Nov. 1960, pp. 1865-1870.

3. Schriever, R. L., and Johnson, C. C.:  A Rotating Beam Waveguide Oscillator.  Proc. IEEE, vol. 54, 1966, pp. 2029-2030.

4. Bott, I. B.:  A Powerful Source of Millimeter-Wavelength Electromagnetic Radiation.  Phys. Letters, vol. 14, Feb. 1965, pp. 293-294.

5. Chow, K. K., and Pantell, R. H.:  A Small-Signal Analysis of the Electron Cyclotron Backward-Wave Oscillator.  Trans. IEEE, vol. ED-9, July 1962, pp. 351-358.

6. Schriever, R. L., Durney, C. H., Johnson, C. C., and Grow, R. W.:  Transverse-Wave Interactions between Rotating Electron Beams and Waveguides, Technical Report #6, Dept. of Electrical Engineering, University of Utah, Salt Lake City, Utah, April 1968.

7. Hsu, T. W.:  Coherent Millimetre-Wave Cyclotron Radiation from Relativistic Electrons.  Doctoral Thesis, Dept. of Electronic and Electrical Engineering, University of Sheffield, Sheffield, England, August 1966.

8. Hsu, T. W., and Robson, P. N.: Negative Absorption from Weakly Relativistic Electrons Traversing a Cuccia Coupler. Electronics Letters, vol. 1, no. 4, June 1965, pp. 84-85.

9. Hirshfield, J. L., Bernstein, I. B., and Wachtel, J. M.: Cyclotron Resonance Interaction of Microwaves with Energetic Electrons. IEEE J. Quantum Electronics, vol. QE-1, Sept. 1965, pp. 237-245.

10. Beasley, J. P., An Electron Cyclotron Resonance Oscillator at Millimetre Wavelengths. Paper given at the 6th Int. Conf. on Microwave and Optical Generation and Amplification (MOGA), Cambridge, England, 1966.

11. Gaponov, A. V., et al.: Induced Synchrotron Radiation of Electrons in Cavity Resonators, JETP Letters, vol. 2, Nov. 1, 1965, pp. 267-269.

12. Antakov, I. I., Gaponov, A. V., Malygin, O. V., and Flyagin, V. A.: Application of Induced Cyclotron Radiation of Electrons for the Generation and Amplification of High-Powered Electromagnetic Waves. Radio Engr. and Elect. Phys., vol. 11, 1966, pp. 1995-1998.

13. Sehn, G. J.: Relativistic Interaction between a Slow, Rotating Electron Beam and a Microwave Field inside a Waveguide at the Cyclotron Frequency. Doctoral Thesis, Dept. of Electrical Engineering, University of Colorado, Boulder, CO., Sept. 1967.

14. Sehn, G. J., and Hayes, R. E.: Relativistic Effect in Electron Cyclotron Transverse-Wave Devices. <u>Trans. IEEE</u>, vol. ED-16, Dec. 1969, pp. 1077-1078.

15. McIsaac, P. R.: Research into Advanced Concepts of Microwave Power Amplification and Generation Utilizing Linear Beam Devices, Semiannual Status Reports, School of Electrical Engineering, Cornell University, NASA Research Grant NGL-33-010-047, Dec. 1967 through Dec. 1969.

16. Lindsay, P. A., Cyclotron Resonance Interaction-Classical and Quantum-Mechanical Treatments Compared, 7th Int. Conf. Microwave and Optical Generation and Amplification, Amsterdam, Holland, Sept. 1970.

17. Kulke, B.: Design Considerations for Cyclotron Resonance Oscillators. NASA TN D-5237, June, 1969. Also, Kulke, B., and Wilmarth, R. W.: Small-Signal and Saturation Characteristics of an X-band Cyclotron-Resonance Oscillator. <u>Proc. IEEE (letters)</u>, vol. 57, February 1969, pp. 219-220.

18. Rowe, John F.: A Large-Signal Analysis of the Cyclotron-Resonance Oscillator. Doctoral Dissertation, Dept. of Electrical Engineering, Cornell Univ., Ithaca, N. Y., January 1970.

19. Schneider, J.: Stimulated Emission of Radiation by Relativistic Electrons in a Magnetic Field, <u>Phys. Rev. Letters</u>, vol. 2, June 1959, pp. 504-505.

20. Chodorow, M., and Wessel-Berg, T.:  A High-Efficiency Klystron with Distributed Interaction.  _IRE Trans. on Electron Devices_, ED-8, Jan. 1961, pp. 44-55.

21. Pierce, J. R.:  _Theory and Design of Electron Beams_, Van Nostrand, New York, 1954, p. 167.

22. Collin, R. E.:  _Foundations for Microwave Engineering_, McGraw Hill Co., New York, 1966, p. 327.

23. Wingerson, R. C.:  "Corkscrew" - A Device for Changing the Magnetic Moment of Charged Particles in a Magnetic Field. _Phys. Rev. Letters_, vol. 6, May 1, 1961, pp. 446-448.

24. Kulke, B.:  Energy Distribution of a Spiraling Electron Beam. NASA Technical Note TN D-5490, Nov. 1969.  Also, _Proc. IEEE_ (Letters), vol. 58, March 1970, pp. 487-488.

25. Kulke, B.:  Application of a Magnetic-Mirror System as a Velocity Analyzer.  Rev. Sci. Inst., June 1971 (approx.).

26. Ginzton, E. L.:  _Microwave Measurements_, McGraw-Hill, New York, 1957, Ch. 9.

27. Siegman, A. E.:  _Microwave Solid-State Masers_ McGraw-Hill, New York, 1964, p. 259.

28. Ibid., Fig. 6-35.

29. Landau, L.:  Diamagnetismus der Metalle, Z. J. Physik, vol. 64, 1930, pp. 629-637.